

## On the Development of SWOT In Situ Calibration/Validation for Short-Wavelength Ocean Topography

JINBO WANG,<sup>a</sup> LEE-LUENG FU,<sup>a</sup> BRUCE HAINES,<sup>a</sup> MATTHIAS LANKHORST,<sup>b</sup> ANDREW J. LUCAS,<sup>b,c</sup> J. THOMAS FARRAR,<sup>d</sup> UWE SEND,<sup>b</sup> CHRISTIAN MEINIG,<sup>e</sup> OSCAR SCHOFIELD,<sup>f</sup> RICHARD RAY,<sup>h</sup> MATTHEW ARCHER,<sup>a</sup> DAVID ARAGON,<sup>f</sup> SEBASTIEN BIGORRE,<sup>d</sup> YI CHAO,<sup>g</sup> JOHN KERFOOT,<sup>f</sup> ROBERT PINKEL,<sup>b</sup> DAVID SANDWELL,<sup>b</sup> AND SCOTT STALIN<sup>e</sup>

<sup>a</sup> *Jet Propulsion Laboratory, California Institute of Technology, Pasadena, California*

<sup>b</sup> *Scripps Institution of Oceanography, University of California, San Diego, La Jolla, California*

<sup>c</sup> *Department of Mechanical and Aerospace Engineering, University of California, San Diego, La Jolla, California*

<sup>d</sup> *Woods Hole Oceanographic Institution, Woods Hole, Massachusetts*

<sup>e</sup> *Pacific Marine Environmental Laboratory, National Oceanic and Atmospheric Administration, Seattle, Washington*

<sup>f</sup> *Rutgers, The State University of New Jersey, New Brunswick, New Jersey*

<sup>g</sup> *Remote Sensing Solutions, Monrovia, California*

<sup>h</sup> *NASA Goddard Space Flight Center, Greenbelt, Maryland*

(Manuscript received 7 April 2021, in final form 10 November 2021)

**ABSTRACT:** The future Surface Water and Ocean Topography (SWOT) mission aims to map sea surface height (SSH) in wide swaths with an unprecedented spatial resolution and subcentimeter accuracy. The instrument performance needs to be verified using independent measurements in a process known as calibration and validation (Cal/Val). The SWOT Cal/Val needs in situ measurements that can make synoptic observations of SSH field over an  $O(100)$  km distance with an accuracy matching the SWOT requirements specified in terms of the along-track wavenumber spectrum of SSH error. No existing in situ observing system has been demonstrated to meet this challenge. A field campaign was conducted during September 2019–January 2020 to assess the potential of various instruments and platforms to meet the SWOT Cal/Val requirement. These instruments include two GPS buoys, two bottom pressure recorders (BPR), three moorings with fixed conductivity–temperature–depth (CTD) and CTD profilers, and a glider. The observations demonstrated that 1) the SSH (hydrostatic) equation can be closed with 1–3 cm RMS residual using BPR, CTD mooring and GPS SSH, and 2) using the upper-ocean steric height derived from CTD moorings enable subcentimeter accuracy in the California Current region during the 2019/20 winter. Given that the three moorings are separated at 10–20–30 km distance, the observations provide valuable information about the small-scale SSH variability associated with the ocean circulation at frequencies ranging from hourly to monthly in the region. The combined analysis sheds light on the design of the SWOT mission postlaunch Cal/Val field campaign.

**KEYWORDS:** Internal waves; Ocean dynamics; Small scale processes; Altimetry; Global positioning systems (GPS); In situ oceanic observations; Ship observations

### 1. Introduction

The Surface Water and Ocean Topography (SWOT) mission is a pathfinder mission that will demonstrate the next-generation satellite altimeter based on a Ka-band radar interferometer (KaRIn) (Durand et al. 2010; Fu and Ubelmann 2014). The major thrusts of the mission are the low noise and wide-swath sea surface height (SSH) measurements of the KaRIn instrument. After its launch in 2022, understanding the performance of the KaRIn instrument against a ground truth of dynamical SSH is crucial for subsequent scientific applications. This emphasizes the importance of the mission's ocean topography calibration and validation (Cal/Val), which focuses on the wavenumber spectrum of SWOT SSH measurement errors.

In the past, the ground truth for satellite altimeters was typically produced using point measurements from ground stations such as tide gauges, a method that has been used

successfully for all previous nadir-altimeter missions, such as the Jason-series altimeters (e.g., Haines et al. 2021; Bonnefond et al. 2019; Quartly et al. 2021). However, the SWOT mission requires a new approach for calibration and validation because the SWOT science requirement is specified in terms of the wavenumber spectrum over 15–1000 km wavelengths (Fig. 1; Desai et al. 2018). As such, validation of the sensor requires capturing a synoptic SSH field along a line covering 15–1000 km wavelengths. Validation of wavelengths ranging from ~120 to 1000 km will be accomplished by the onboard Jason-class altimeter (Wang and Fu 2019), whose performance in wavenumber space is known (e.g., Dufau et al. 2016). The ground truth over the short wavelength (15–150 km) may be achieved by airborne instruments such as lidar (Melville et al. 2016) for geodetic validation and in situ oceanographic measurements (Wang et al. 2018) for oceanographic validation. For the latter, we need an observing approach designed specifically for SSH wavenumber spectrum validation at scales between 15 and 150 km with subcentimeter accuracy.

Corresponding author: Jinbo Wang, jinbo.wang@jpl.nasa.gov

DOI: 10.1175/JTECH-D-21-0039.1

© 2022 American Meteorological Society. For information regarding reuse of this content and general copyright information, consult the AMS Copyright Policy ([www.ametsoc.org/PUBSReuseLicenses](http://www.ametsoc.org/PUBSReuseLicenses)).

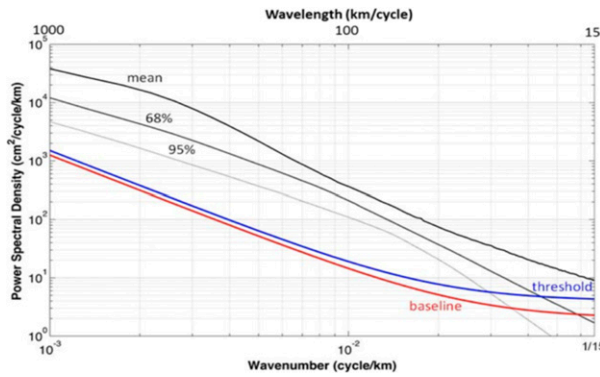


FIG. 1. The SSH baseline requirement spectrum (red line) as a function of wavenumber (Desai et al. 2018). The thick black line is the mean spectrum of the Jason-2 altimeter track 159, which extends from the Southern Ocean to North Pacific. The 68th and 95th percentiles are marked by the thin black line and the gray line; i.e., 68% and 95% of the spectra are above the corresponding curve. The red curve defines the baseline requirement represented by  $E(k) = 2 + 0.00125k^{-2}(\text{cm}^2 \text{cpkm}^{-1})$ . The blue curve represents the threshold requirement  $E(k) = 4 + 0.0015k^{-2}(\text{cm}^2 \text{cpkm}^{-1})$ .

An observing system simulation experiment (OSSE) was conducted as a first step to evaluate the feasibility of an array of moorings to meet the Cal/Val requirement (Wang et al. 2018). Based on the OSSE, the top challenges in reconstructing the small-scale synoptic SSH field over a 150 km distance come from the emerging dominance of superinertial high-frequency SSH variability at spatial scales  $<150$  km, and the weak SSH signal itself at those scales. These challenges led to a series of field campaigns to identify the relevant ocean processes at the Cal/Val site (near  $35.6^\circ\text{N}$ ,  $125^\circ\text{W}$ ) and to evaluate the performance of different in situ platforms and instruments in meeting the SWOT requirement.

Here we report the results from a recent field campaign conducted between September 2019 and January 2020. The rest of the paper is organized as follows. Section 2 summarizes the past development of SWOT oceanographic Cal/Val and the in situ field campaigns. The summary provides the background and motivation of this study. Section 3 discusses the instrumentation of the 2019/20 field campaign. Results are shown in section 4. Uncertainties in the observations and quantifications exist and are discussed in section 5. Summaries are presented in section 6.

## 2. The development of SWOT SSH Cal/Val

This section reviews the previous work in developing an in situ observing array for the SWOT oceanographic Cal/Val. Section 2a introduces the nature of the SWOT SSH Cal/Val. Section 2b discusses the theoretical basis for conducting oceanographic Cal/Val through in situ mooring platforms. Section 2c reviews the previous OSSE results. Section 2d discusses the transformation of the measurement errors from wavenumber spectrum to time series measurement at a single point and provides accuracy requirements imposed on individual observing platforms used in the field campaign. Section 2e

briefly reviews a pilot field campaign that took place prior to the recent 2019/20 field campaign.

### a. SWOT SSH Cal/Val

After the SWOT satellite launch, the first 90 days will be dedicated to instrument hardware checkout. The second 90 days will be for the mission Cal/Val along a 1-day-repeat orbit (Desai et al. 2018). The 90-day Cal/Val orbit provides more frequent SSH measurements at certain locations for both the validation of the instrument and to develop an understanding of the SWOT measurements from an oceanographic perspective at a very early stage. The SWOT mission Cal/Val has two aspects: 1) characterizing the performance of the instrument KaRIn from a geodetic perspective and 2) characterizing the SWOT-observed variability from an oceanographic perspective.

Recent studies have shown that the superposition of eddies and internal gravity waves in SSH may make the interpretation of SWOT observations complicated (Rocha et al. 2016; Qiu et al. 2018; Torres et al. 2018; Morrow et al. 2019). When considering the exploratory nature of the SWOT mission as the next-generation altimeter, it is crucially important that we use this 1-day repeat fast-sampling period, in which the satellite will overfly ground-track crossover region twice a day. The results will shed light on the connection of the SWOT SSH to the dynamics of ocean circulation beneath the sea surface (e.g., d'Ovidio et al. 2019), which is the mission's ultimate science goal for oceanography.

### b. Closing the SSH budget using in situ observations

The ocean dynamics governing the large and mesoscale SSH variability have been the subject of intensive research over the past few decades, stimulated in part by satellite altimetry (e.g., Fu and Cazenave 2001). The SSH signal that has spatial scales smaller than mesoscale, however, has not yet been fully explored, largely because of lack of observations. The first task is to understand the observability of SSH at scales of  $\sim 150$  km and smaller. To what level of accuracy can we close the SSH budget (formulated below) using available in situ instruments and platforms?

Integrating the hydrostatic equation  $dp/dz = \rho g$  from the ocean floor to the free surface, the SSH budget equation can be written as

$$p(-H) = \int_{-H}^{\eta} g\rho(z) dz + p_a,$$

in which  $-H$  is the depth of the ocean floor,  $\eta$  is the free sea surface height,  $p_a$  is the atmospheric pressure. We are interested in the temporal variability. Decomposing each term into a temporal mean (overline) and an anomaly (prime) gives

$$\begin{aligned} \bar{p}(-H) &= \int_{-H}^0 g\bar{\rho}(z) dz + g\rho_0\bar{\eta} + \bar{p}_a, \\ p'(-H) &= \int_{-H}^0 g\rho' dz + g\rho_0\eta' + p'_a, \end{aligned} \quad (1)$$

where  $\rho_0$  the reference density,  $\rho'$  the in situ density anomaly,  $\eta'$  the sea surface height anomaly referenced to  $\bar{\eta}$ ,  $p'_a$  the

atmospheric pressure anomaly. The term  $g\eta'\rho'$  is second order and neglected.  $\bar{\eta}\rho'$  is implicitly included in the first term on the right hand by taking  $z = 0$  at  $\bar{\eta}$ . The four terms in Eq. (1) represent temporal anomalies of bottom pressure, dynamic height, sea surface pressure due to the free surface, and atmospheric pressure. These terms from left to right can be assessed by bottom pressure recorders (BPR), moorings with CTDs, GPS buoys, and barometers, respectively. We test the closure of Eq. (1) using GPS, BPR, and mooring CTDs in section 4b.

Note that the dominant variability in both the bottom pressure and the free sea surface elevation is nonsteric, such as the barotropic tides. The steric component is much weaker, typically only on the order of a few centimeters.

Denote the steric and nonsteric components of the sea surface height and bottom pressure as  $\eta'$ ,  $\eta'_{ns}$ ,  $p'_{bs}$ , and  $p'_{bns}$ , respectively. We further expand Eq. (1) into

$$p'_{bs} + p'_{bns} = \int_{-H}^0 g\rho' dz + g\rho_0 s'_\eta + g\rho_0 \eta'_{ns} + p'_a. \quad (2)$$

The cancellation of the nonsteric components is written as  $p'_{bns} = g\rho_0 \eta'_{ns} + p'_a$ . After removing the nonsteric components, Eq. (2) becomes

$$p'_{bs} - g\rho_0 \eta'_s = \int_{-H}^0 g\rho' dz. \quad (3)$$

Equation (3) means that the dynamic height due to the density change can be calculated directly from density profiles or indirectly calculated from bottom pressure and steric sea surface height (after the atmospheric pressure correction). In reality, the steric and nonsteric components are impossible to separate from bottom pressure or GPS free sea surface based on a single mooring as a result of an underdetermined problem. Equation (3) is only used to illustrate the meaning of the closure of the SSH equation. It is worth noting that deriving  $O(1)$  cm steric height from  $O(100)$  cm GPS SSH and BP-derived SSH requires extreme accuracy in both instruments. For this reason, one of the objectives of the SWOT pre-launch campaigns (sections 2e and 3) was to examine the closure of the hydrostatic equation [Eq. (1)] and to quantify the errors associated with different platforms and instruments.

### c. An OSSE

An OSSE was first conducted to understand the SSH signal at SWOT scales and the performance of different instruments and platforms in meeting the SWOT requirement (Wang et al. 2018). We used a tide-resolving high-resolution global ocean simulation as a virtual ocean and simulated the performance of several instruments/platforms commonly used in modern observational physical oceanography, i.e., underway CTDs (UCTD), gliders, fixed-CTD moorings, pressure inverted echo sounders (PIES). The model simulation is the high-resolution global ocean simulation using MITgcm with  $1/48^\circ$  horizontal resolution, llc4320, used in several recent studies (e.g., Rocha et al. 2016; Torres et al. 2018; Su et al. 2018; Yu et al. 2019). One conclusion was that

in the Cal/Val region (near  $35.7^\circ\text{N}$ ,  $124.7^\circ\text{W}$ ) the total SSH over the 15–150 km wavelength range (SWOT scale) can be represented by the upper-ocean steric height after the large-scale barotropic signal and inverted barometer (IB) influence are removed through a high-pass filter. The residual is well below the mission error requirement shown in the error wavenumber spectrum in the OSSE study.

The OSSE study also found that internal gravity waves and internal tides (IGW) might be strong enough to mask the eddy field SSH signal over the small spatial scales and impose an observational challenge (Wang et al. 2018). This dominance of IGWs over small scales is simply because the SSH wavenumber spectrum of eddies (balanced motions) is steeper than that of IGWs (Qiu et al. 2018; Chereskin et al. 2019; Callies and Wu 2019). The presence of internal gravity wave motions on these scales poses a challenge for designing an in situ observational network. For example, through the OSSE we found that slow platforms such as ship-towed UCTD are unable to meet the Cal/Val requirement. An array of station-keeping gliders can marginally meet the requirements, but the errors are mostly over small spatial scales ( $\sim 50$  km) due to the high-frequency motions. PIES can empirically convert the travel time of an acoustic signal to steric height but have about 5 cm uncertainty (D. R. Watts 2016, personal communication; Wang et al. 2018), which is larger than SWOT's subcentimeter requirement. The OSSE study concluded that an array of CTD-equipped moorings could produce a steric height field that is sufficiently accurate to meet the requirement.

The numerical ocean simulation used in the OSSE, however, has excessive tidal energy (C. Wunsch 2017, personal communication; Savage et al. 2017; Yu et al. 2019), which introduces large uncertainties in the OSSE results. It is also not clear how well the deep-ocean variability is reproduced. Field experiments are necessary to test the performance of different platforms and instruments. In addition, while the OSSE focused on oceanographic Cal/Val, the geodetic SSH such as measured by GPS buoys needs to be evaluated to synthesize the oceanographic and geodetic objectives. It led to two objectives of the field campaigns: 1) quantify the performance of oceanographic in situ platforms and 2) test the GPS measurements and their relationship with those derived from hydrographic measurements.

### d. SWOT measurement error requirement

In the two field campaigns described in the next section, we do not have a full-scale mooring array that enables a wavenumber spectrum calculation. To evaluate the performance of an in situ instrument, the SWOT error requirement in wavenumber space needs to be integrated over a range of wavenumbers  $\int E(k)$  to assess time series in situ measurement. The mission requirement is specified between 15 and 1000 km wavelengths. The baseline error<sup>1</sup> is

<sup>1</sup> The "baseline error" is the error the mission currently plans to achieve. The "threshold error" is the error level that the mission must achieve to address the minimum science goals.

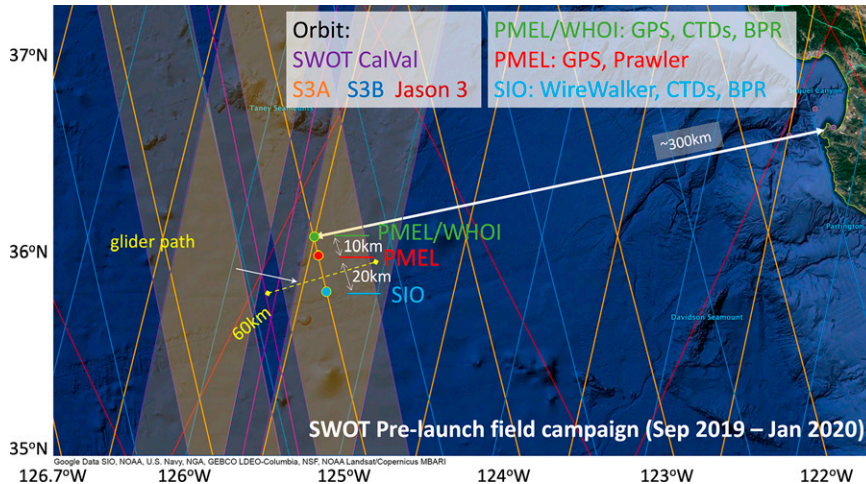


FIG. 2. Map of the field campaign instrumentation. The three moorings are marked by the three colored dots. From north to south, they are the PMEL/WHOI mooring, the PMEL Prawler mooring with GPS on the buoy, and the SIO full-depth mooring. The separation distance is 10 and 20 km. The dashed yellow line is the glider target path of 60 km wide. Two bottom pressure recorders were deployed near the PMEL/WHOI and SIO moorings.

$E(k) = 4 \text{ cm}^2 \text{ cpkm}^{-1} + 0.00125k^{-2}$ , where  $k$  is the wavenumber with a unit of cycle  $\text{km}^{-1}$  (cpkm) and  $2 \text{ cm}^2 \text{ cpkm}^{-1}$  is the KaRIn instrument noise averaged across a swath over 7.5 km distance for significant wave height (SWH) of 2 m (Fig. 1, red line). The threshold error requirement is similar:  $E(k) = 4 \text{ cm}^2 \text{ cpkm}^{-1} + 0.0015k^{-2}$  (Fig. 1, blue line).

For the spatial range between 15 and 1000 km, an integration of the error based on the requirement is  $\int_{1 \times 10^{-3}}^{1/15} E(k) dk = 1.36 \text{ cm}^2$ , i.e., 1.17 cm RMS. If only the 15–150 km range is considered, the total integrated error has 0.29  $\text{cm}^2$  variance (0.54 cm RMS), the integrated random KaRIn noise is 0.12  $\text{cm}^2$  (0.35 cm RMS), and the integrated correlated error (cpkm) is 0.17  $\text{cm}^2$  (0.41 cm RMS). The 0.54 cm number represents a target accuracy needed for validating SSH measurements in the presence of oceanographic “noise,” i.e., an upper limit for errors in observing ocean processes including those which are correlated on the scales of interest. These are the signals analyzed in this study. The 0.35 cm value is a requirement for inherent sensor/platform/sampling error at a single location that is uncorrelated from platform to platform.

The postlaunch Cal/Val approach involves calculating the wavenumber spectrum of the difference between the SWOT SSH measurement and the mooring-derived SSH during the SWOT overflight of the mooring array. A spatial linear trend over the length of the mooring array will be removed before calculating the wavenumber spectrum. This detrending operation minimizes the effects of the scales longer than those of the in situ Cal/Val. Such a difference spectrum is considered a snapshot of the measurement error spectrum, which will be averaged over the 90-day Cal/Val period to achieve statistical assessment of the SWOT performance.

Ideally, we would like to test the mooring capability using an array of moorings covering  $\sim 150$  km. However, owing to the limited budget, we deployed three moorings spanning 30 km (Fig. 2). The evaluation of the mooring capability

discussed in the following sections will be unavoidably influenced by the large-scale signals that are irrelevant to SWOT short-wavelength Cal/Val. It is thus difficult to rigorously define measurement requirement for a single mooring. However, from analysis of ocean model simulations (Torres et al. 2018), the temporal scales corresponding to 15–150 km wavelengths are roughly 2–14 days. We therefore impose the following for the requirement for the in situ SSH observations: Integrated over periods of 2–14 days, the RMS error shall not exceed 0.54 cm. A caveat is that this criterion is not rigorously derived due to insufficient mooring measurements and is only used as a guideline. The spatial–temporal separation can be directly calculated during the postlaunch Cal/Val where an order of 10 moorings will be deployed along a line under a SWOT swath (section 5).

#### e. The 2017 pilot field campaign

The first field campaign was conducted in Monterey Bay, California, during June/July 2017. Two gliders, one BPR, and a GPS buoy (Haines et al. 2017) were deployed near the Monterey Bay Aquarium Research Institute (MBARI)  $M_1$  mooring. The two gliders sampled the upper 500 m near the mooring at 36.75°N, 122.03°W. The first objective was to quantify the capability of station-keeping gliders in constructing the high-resolution steric height derived from a fixed instrumented mooring. The second objective was to examine the connection between GPS-observed SSH that resembles spaceborne measurements and steric height that represents the ocean circulation.

The 2017 pilot campaign successfully tested the first objective, but not the second one. In particular, the results have not yet yielded satisfying closure between the GPS-derived SSH and upper-ocean steric height. The campaign took place on the steep walls of the Monterey submarine canyon. One of the

challenges was the large mean sea surface (geoid) gradient, which contributes to the time variation in GPS-derived SSH as the buoy meandered over the canyon wall and within the watch circle. This nearshore location was also dominated by nonsteric processes, making the site less representative of the open-ocean conditions expected near the SWOT Cal/Val crossover location. The campaign, however, shed new light on the challenges of reconciling SSH (from surface GPS or satellites such as SWOT) with steric height (from gliders and moorings), and the outcomes helped to inform the architecture of the subsequent 2019/20 prelaunch campaign reported in this paper. The next section provides the general information about this campaign.

### 3. The 2019/20 prelaunch field campaign

The 2019/20 prelaunch field campaign was conducted near the SWOT Cal/Val crossover location, about 300 km west of Monterey, California (Fig. 2), between September 2019 and January 2020. It was designed to mainly 1) test the closure of the SSH equation, which was not satisfactorily addressed in the 2017 field campaign, and 2) quantify the error in steric height using different platforms. There are six specific objectives: 1) test the SSH budget closure with GPS buoy, CTD mooring, and BPR following Eq. (1); 2) evaluate the vertical scale of SSH at the SWOT scales for different frequency bands; 3) evaluate the role of bottom pressure in SWOT SSH signals; 4) evaluate the small-scale steric height information; 5) evaluate the reconstruction of the upper-ocean circulation; and 6) provide information for the design of the postlaunch in situ observing system. We will mainly focus on 1–4 in this paper. The outcome will aid the design of the postlaunch in situ field campaign for SWOT Cal/Val.

Six institutions participated in the campaign: Jet Propulsion Laboratory, NOAA Pacific Marine Environmental Laboratory, Wood Hole Oceanographic Institution, Scripps Institution of Oceanography, Rutgers, and Remote Sensing Solutions. Three moorings and two BPRs were deployed between 1 and 7 September 2019, and recovered between 16 and 21 January 2020. One Slocum glider was deployed from Monterey Bay and piloted to the mooring locations around mid-September 2019.

The three moorings are 1) the PMEL/WHOI (*northern mooring*) configured with a GPS buoy and 18 fixed CTDs from surface to the bottom, 2) the PMEL GPS mooring (*middle mooring*) with a Prawler (Osse et al. 2015) sampling the upper-500-m temperature and salinity (*T/S*), and 3) the Scripps Institution of Oceanography (SIO) mooring (*southern mooring*) with a Wirewalker (Pinkel et al. 2011) sampling the top 500 m and fixed, real-time telemetered CTDs between 500 m and ocean floor. The mooring array was placed along a *Sentinel-3A* ground track, which fortuitously was in the middle of a SWOT swath along the Cal/Val orbit. The separation distances are 10 and 20 km for the northern and southern pairings, respectively, to support testing of small-scale SSH variability not resolved by conventional satellite altimeters. During the first phase of the campaign, the glider sampled a 60-km-long section perpendicular to the mooring line (Fig. 2)

with a 1000 m dive depth, which was chosen to minimize the travel time for the 60 km section. During the second phase, the glider performed station keeping near the three moorings for cross calibration. The glider stayed at each mooring for about 5 days. The PMEL BPR is near the northern mooring and a PIES was deployed at the southern mooring location.

#### a. GPS measurements of SSH

A modular, low-power, high-accuracy GNSS measurement system was designed for long-term, continuous, and autonomous measurements of SSH on ocean- and cryosphere-observing platforms (Haines et al. 2017; Guthrie et al. 2020). It results from a joint project between NASA JPL, NOAA PMEL, and the University of Washington. The project aims to probe the limit of new kinematic precise-point positioning (PPP) techniques for accurately determining sea surface height and recovering neutral and charged atmosphere characteristics; and explore the potential scientific benefits—in the fields of physical oceanography, weather, and space weather—of accurate GNSS observations from a global ocean network of floating platforms. It integrates a Septentrio dual-frequency GPS receiver and a PMEL buoy. The receiver is low power (~1 W) and is accompanied by a miniaturized digital compass (for attitude information) and a load cell (to measure force on the mooring line). The buoy communicates using Iridium, and the payload is adaptable to multiple floating platforms such as surface buoys, wave gliders. When coupled with advanced precise point positioning techniques (Bertiger et al. 2010), the observations collected by the GPS buoy enable geodetic-quality solutions in remote locations without nearby reference stations.

The GPS level-2 data have 1-Hz temporal frequency, processed to accurate 3D positions using the GipsyX software (Bertiger et al. 2020) with units of meters for the height component. These high-frequency data were binned to hourly average to remove the surface gravity waves (Fig. 3). The hourly data were then corrected for an apparent systematic sea-state bias (estimated empirically), solid tides, line tension, mean sea surface (MSS), and IB effect. The MSS correction is important for comparing GPS-SSH with steric height because the horizontal displacement of the GPS buoy within its watch circle can project geoid variations into the GPS time series. This spatial-to-temporal projection is especially significant over steep bathymetry, which was the case during the 2017 field campaign, where the GPS buoy was placed near the Monterey submarine canyon and the spatial geoid variations were as large as 10 cm within the mooring watch circle of 2 km radius, but less significant over the prelaunch campaign region where ocean bathymetry is rather flat. The IB correction (Wunsch and Stammer 1997) follows  $IB \text{ (mm)} = -9.948p'$ , where  $p'$  is the sea level pressure anomaly. The final derived SSH after the MSS and IB corrections was then detrended over the 4-month period (mid-September 2019 to mid-January 2020).

The GPS buoy system has developed from campaigns undertaken in progressively more challenging conditions.

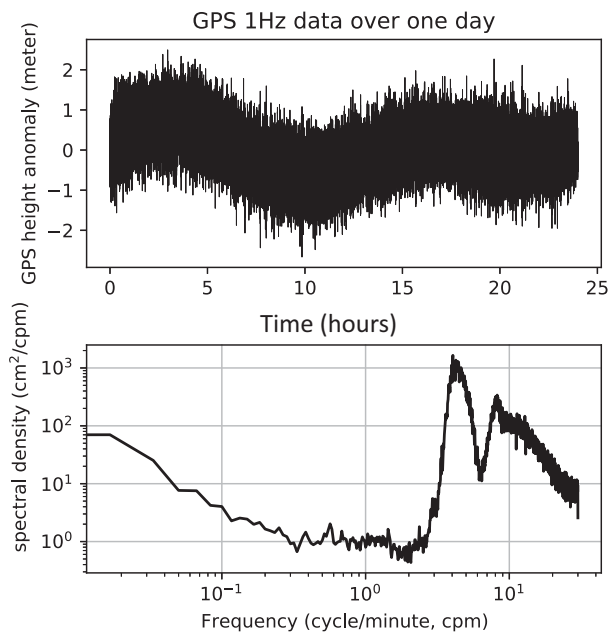


FIG. 3. (top) The 1-Hz GPS measurement of SSH. (bottom) The frequency spectrum of the 1-Hz GPS SSH.

Nearly 1000 buoy days of data have been successfully collected since 2015, over SWH ranging from calm to 9 m. The GPS buoys have been an integral part of the SWOT pilot experiment in 2017 (Monterey Bay) and the prelaunch field campaign (2019/20). An example of the processed 1-Hz data is shown in Fig. 3. The 1-Hz sampling frequency is high enough to reveal detailed expressions of surface waves. The amplitude of the high-rate (1-Hz) height estimates reach 5 m for this day. The frequency spectrum illustrates the wind wave and swells by the two spectral peaks. SWH can also be derived from this 1-Hz data following  $SWH = 4 \times \text{RMS}(\text{SSH})$ , where SSH is high-pass filtered with a cutoff frequency of  $1 \text{ cycle min}^{-1}$ .

We tried to estimate the GPS measurement errors in the context of the SWOT requirements. Without a true reference, we need to make assumptions in order to derive the error from the GPS measurement itself. We assume the minimum in the spectrum near  $1 \text{ cycle min}^{-1}$  reflects random instrument noise. As we are interested in ocean signals that are of periods longer than 1 h, the GPS error can be estimated by integrating the random noise spectrum, assumed constant taken as the value of the spectrum minimum near  $1 \text{ cycle min}^{-1}$ , over the frequency range ( $0\text{--}1 \text{ cycle h}^{-1}$ ). The SWH can be derived from the surface wave spectrum. We can split a long time series into 1-h-long segments, then derive an empirical relationship between GPS error and SWH. Based on the two SWOT prelaunch field tests, there is a clear relationship between SWH and GPS errors following a logarithmic function as shown in Fig. 4. The relationship is  $S^2 = 10^{-2.31 + 0.301H_{m0}}$ , where  $H_{m0}$  represents the SWH, and  $S^2$  is the noise variance. Under these assumptions, the GPS error from a single buoy meets the SWOT mission geodetic requirement, i.e.,  $0.13 \text{ cm}^2$

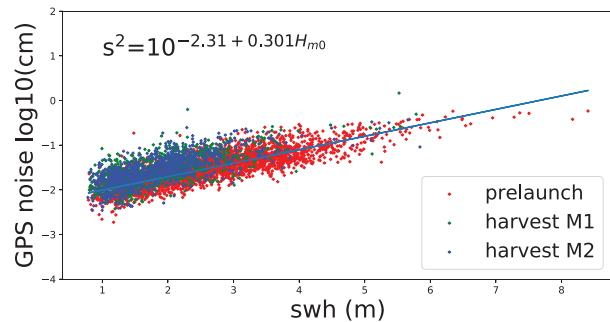


FIG. 4. The GPS error as a function of SWH derived from two SWOT prelaunch field campaigns described in section 2. The red dots are from the 2019 prelaunch field campaign and the green and blue dots are from the two GPS buoys of the 2017 pilot field campaign.

for  $SWH < 4.1 \text{ m}$ , which corresponds to  $2 \text{ cm}^2 \text{ cpm}^{-1}$  instrument noise in the wavenumber space (Fig. 1).

Other errors exist in addition to those induced by the surface waves. Those errors are correlated but difficult to unravel with a single GPS buoy. They will contribute to the total error presented in section 4. Residual atmospheric refraction delays are one of the dominant correlated error sources. As the ionospheric refraction is corrected to first order using the two GPS frequencies, the primary concern here is refraction from the troposphere. Taking advantage of mapping functions, the wet troposphere delay in the zenith direction is estimated along with the buoy position. Despite the relatively small magnitude, the wet component of the troposphere delay is highly variable and sometimes difficult to capture, especially during intense weather fronts with large atmospheric gradients. Other important systematic errors for the buoy technique are related to the platform altitude and to the force on the mooring line, both of which impact accurate modeling of the buoy's waterline and thus the SSH (Zhou et al. 2020). Here we use, respectively, the digital compass and load cell data from our payload package to mitigate these errors.

## b. Hydrographic measurements

### 1) MOORINGS WITH FIXED-DEPTH CTD INSTRUMENTATION

The fixed-depth CTD mooring is one of the most conventional in situ platforms for observational oceanography. The CTDs used in the campaign are the Sea-Bird Electronics, model SBE-37. The SBE-37 can be configured with and without a pressure sensor. The pressures for those instruments without the corresponding sensors (from the northern mooring) were determined through interpolating from the next instruments above or below, using the known wire lengths between the instruments. For these fixed-depth CTDs, the distances between instruments along the mooring line are fixed, but the actual depths of the CTD instruments change over time. The amount of vertical excursion depends on the currents and winds as well as the mooring design: the northern mooring was a “slack mooring” (i.e., mooring line much longer than

water depth) of an inverse catenary design with vertical sensor excursions up to about 300 m, while the southern mooring had a taut lower section that limited vertical excursions to about 60 m. The nominal depths of the fixed CTDs are (505, 618, 810, 1182, 1690, 2365, 3202, 4384) m on the southern mooring and (20, 30, 59, 107, 174, 261, 367, 492, 609, 805, 1180, 1408, 1692, 1909, 2189, 2488, 2750, 4545) m on the northern mooring.

A climatological mean in situ density profile is removed before the density anomalies are interpolated onto a uniform vertical grid to avoid interpolation error in calculating steric height. We have also used the mean profile constructed from all the measurements in the campaign instead of the climatological mean. No quantitative difference is observed. This procedure removes the spurious deep-ocean variability introduced by the vertical-to-temporal projection due to the vertical movement of the CTD sensors. The bottom CTD on the northern mooring was corrupted so the full-depth steric height was calculated with the assumption that the ocean below 3000 m has no temperature and salinity variability.

## 2) MOORINGS WITH PROFILERS

Two moorings had profilers with CTD instruments. The middle mooring had a Prawler that covered the upper 500 m with a Sea-Bird Electronics (SBE-PRAWLER) CTD, and the southern mooring had a Wirewalker in the upper 500 m with an RBR Concerto CTD. Profiling methods are not subject to errors due to vertical resolution, but the temporal resolution is less favorable. The Prawler was set to 8 profiles per day on average during the 2019/20 campaign. The number of profiles per day can be higher, but was chosen to test the endurance of the Prawler mooring. The Wirewalker on the southern mooring yielded about 80 up- and downcast profiles per day (i.e., ~7000 profiles, or 3500 vertical kilometers profiled over 86 days of deployment). The profiler CTDs pass through vertical gradients of temperature and conductivity in the upper ocean, which requires data processing to remove spikes in salinity, and to adjust for lagged sensor responses. After this alignment, vertical profiles of density with 1 and 0.25 m vertical resolution over the upper 500 m are produced for the Prawler and Wirewalker, respectively.

Below the profiler, the southern mooring featured additional, vertical fixed instrumentation. It used a taut mooring between the seafloor and 600 m, connected to the surface buoy via a reverse catenary inductive connection and the Wirewalker profiling wire. The taut mooring has a very small watch circle (<250 m) and so the fixed instruments stay within a narrow depth range. The inductive connection allowed real-time data from the fixed instruments all the way to the seafloor. This experimental mooring design is less tested, and the catenary wire parted after 86 days of the intended 90-day deployment.

## 3) UNDERWATER GLIDERS

The hydrography data collected by the gliders are similar to the moored profilers. Vertical resolution is high and requires no additional interpolation steps, although the same precautions against mismatched sensor response times and resulting spikes in salinity data need to be taken. Gliders have the

advantage of mobility, but they may experience large horizontal deviation from target locations due to strong currents. A station-keeping glider can act as a virtual mooring. A glider that performs station keeping at different mooring locations can also be used for cross-mooring calibration and validation. The Slocum glider used in this campaign has a vertical speed of about 18–20 cm s<sup>-1</sup> yielding ~30 profiles per day for 500 m dives.

## 4) APPROACH TO CALIBRATION AND VALIDATION OF CTD DATA

An effort was made to cross calibrate all CTD data to a common reference. For the fixed-depth, moored CTD instruments, this was done by attaching the mooring instruments to a recently calibrated, ship-based CTD and Rosette system, and then collecting vertical profiles with 10 min stops at several depths. At these dwell depths, water samples were taken for laboratory salinity measurements to provide an absolute salinity reference. This approach was carried out for mooring instruments both before mooring deployment and after mooring recovery. The method is described by [Kanzow et al. \(2006\)](#), and has the key advantage that all three sensors (conductivity, temperature, pressure) are adjusted independently of one another. Over the course of the mooring deployment, the corrections applied to the mooring data are shifted linearly from the predeployment to the postrecovery values. For temperature data, the adjustments are offsets added to the raw data. For conductivity data, the adjustments are gain factors multiplied by the raw data. For pressure data, the adjustments are a combination of a gain factor and an additive offset ([Kanzow et al. 2006](#)).

The glider was flown to the vicinity of each mooring on several occasions. A comparison of the glider data against the fixed-depth, cross-calibrated moored CTDs was used to adjust the glider conductivity with a gain factor, such that the temperature–salinity curves derived from the glider would best match those from the nearby mooring. This assumes that the glider temperature and pressure sensors are correct.

For the two moored profilers, two different approaches were done: The Prawler conductivity data were adjusted against the (adjusted) glider data, based on nudging the conductivity such that the temperature–salinity curves would be matched. For the Wirewalker on the southern mooring, a spare fixed-depth instrument that had the ship-based corrections was attached to the profiling body. The profiler conductivity was nudged against the data from this collocated instrument, again to best match the temperature–salinity relationship, but the comparison was restricted to deeper depths because the fixed-depth instrument does not have a sensor response time suitable for the upper-ocean profiles. For both moored profilers, the result is that the conductivity data are adjusted, while the temperature and pressure data are assumed correct, as for the gliders.

### c. Ocean bottom pressure

There were two ocean bottom pressure instruments: the northern one was a system based on the DART tsunami

detection technology (Meinig et al. 2005), and the southern one a PIES (pressure-sensing inverted echo sounder) (Watts and Rossby 1977). The actual pressure sensors are identical in the two systems (Paroscientific Digiquartz) that are operated at about 15-s acquisition times. The DART-based systems operate nearly continuously, while the PIES have a 10-min sampling interval. When subsampling a near-continuous DART-like record at 10-min resolution, hourly averages can be reproduced to about 0.5 mm accuracy. Availability of the data in near-real time depends on the available underwater communication systems, which typically operate acoustically at low bandwidth. For PIES, hourly data were telemetered on an irregular schedule during the 2017 field campaign, typically with several days' latency. The data transfer uses the nearby glider as a communication device. The northern ocean bottom pressure data were telemetered four times per day during the 2019/20 field campaign using an acoustic modem.

The absolute magnitudes of the pressure data are not particularly useful in the context of SWOT Cal/Val, for two reasons: first, calibration uncertainties typically result in offsets to the data, which are not constant but drift with time; second, the exact depths where the sensors are on the seafloor are not known, i.e., one cannot assign a known vertical coordinate to the data. Therefore, a time mean that includes sensor drift is subtracted from the record. Following Eble and Gonzalez (1991), the preferred trend removal involves the sum of an exponentially decaying function and a linear trend. The variability in the residuals is then dominated by tidal signals. From comparing different tide removal algorithms, such as harmonic fits with different tidal constituents as well as low-pass filters of the data, coherent tidal signals can be removed.

#### d. Auxiliary datasets

GPS measures total SSH, so it is the closest equivalence of SWOT SSH. GPS SSH and SWOT SSH will share the same MSS and IB corrections. For the MSS correction, we used an MSS height model (MSSCNESCLS19), which is based on all available radar altimeter data (Schaeffer et al. 2018) with 16–20 km spatial resolution. The hourly ERA5 atmospheric pressure (Copernicus Climate Change Service 2017; Hersbach et al., 2020) used for IB correction and the gridded DUACS-DT2018 L4 SSH product (Pujol et al. 2016; Taburet et al. 2019) and Sentinel-3A L2P data are provided by Copernicus Climate Change Service (2017).

## 4. Results

### a. Large and mesoscale background during the campaign

The campaign was conducted in the California Current system, a typical eastern boundary current system that comprises a wind-driven coastal upwelling and equatorward surface current. It is one of the best-studied and longest-observed regions in the world oceans (e.g., Hickey 1979; Flament et al. 1985; Ikeda and Emery 1984; Capet et al. 2008a,b; Collins et al. 2013; Rudnick et al. 2017; and many others). The coastal upwelling driven by the equatorward alongshore wind during summer brings cold waters to the surface (Fig. 5d), which

introduces strong thermal fronts next to the warmer open ocean to form a southward California Current. This upwelled water also contains abundant nutrients to support the dynamic ecosystem indicated by the high chlorophyll concentration (Fig. 5e).

Mesoscale and submesoscale eddies are ubiquitous in the California Current System (CCS). The cold coastal water often pinches off from the coastal current and drifts westward into the open ocean supporting the coastal–open-ocean exchange of water masses (e.g., Strub and James 2000, among numerous others). Meanwhile, this offshore transport of mass and heat is balanced by the onshore transport of the deep open-ocean water that feeds the upwelling and the horizontal onshore transport by mesoscale and submesoscale eddies.

During the period of the 2019/20 prelaunch field campaign, the mooring array observed the formation of a warm-core anticyclonic mesoscale eddy. The process started from a southward flow meander at the beginning of the campaign around early September 2019 (Fig. 5a). The meander started to stretch and fold, a typical evolution of baroclinic instability, during October 2019 (Fig. 5b), which eventually detached from the initial meander to form a coherent mesoscale eddy near the end of the campaign (Fig. 5c). The mature mesoscale eddy trapped the warm, nutrient-scarce open-ocean water and drifted shoreward to resupply and mix with coastal water. During this evolution, the three moorings were within the meander at the start of the deployment and on the edge of the formed eddy by the end of the deployment. From the mesoscale perspective, then, the observations during the campaign were skewed toward ocean dynamics of a meander and the edge of a mesoscale eddy in CCS. Detailed in-depth analyses of the underlying mesoscale dynamics are not a focus of this paper and will be reported elsewhere.

### b. SSH closure

As discussed in section 2b, one can derive an equivalent full-depth steric height from GPS, BPR, and atmospheric pressure through the hydrostatic equation. The derived full-depth steric height is then compared with the steric height derived from hydrographic measurements through mooring CTDs. Their differences contain the errors in both GPS-derived and CTD-derived steric heights.

Figure 6 shows the hourly steric height derived from GPS/BPR (red) and 6-min-resolution steric height from hydrographic measurements (blue). The top panel shows the full-time series for four months. The bottom panel shows the details of the time series over a 10-day period. The two independently derived steric height time series agree over low frequencies (top panel) and over major tidal frequencies (bottom panel). Note that the barotropic tides are eliminated by the difference between the GPS SSH and BPR-derived SSH, leaving the residuals at tidal frequencies, the baroclinic internal tides.

The total RMSE between the two derived steric heights is 2 cm, but they also depend on the sea state as shown by the single GPS analyses (Fig. 4). To our knowledge, this is the first demonstration that the GPS-/BPR-derived sea surface height is equivalent to the steric height measured concurrently in

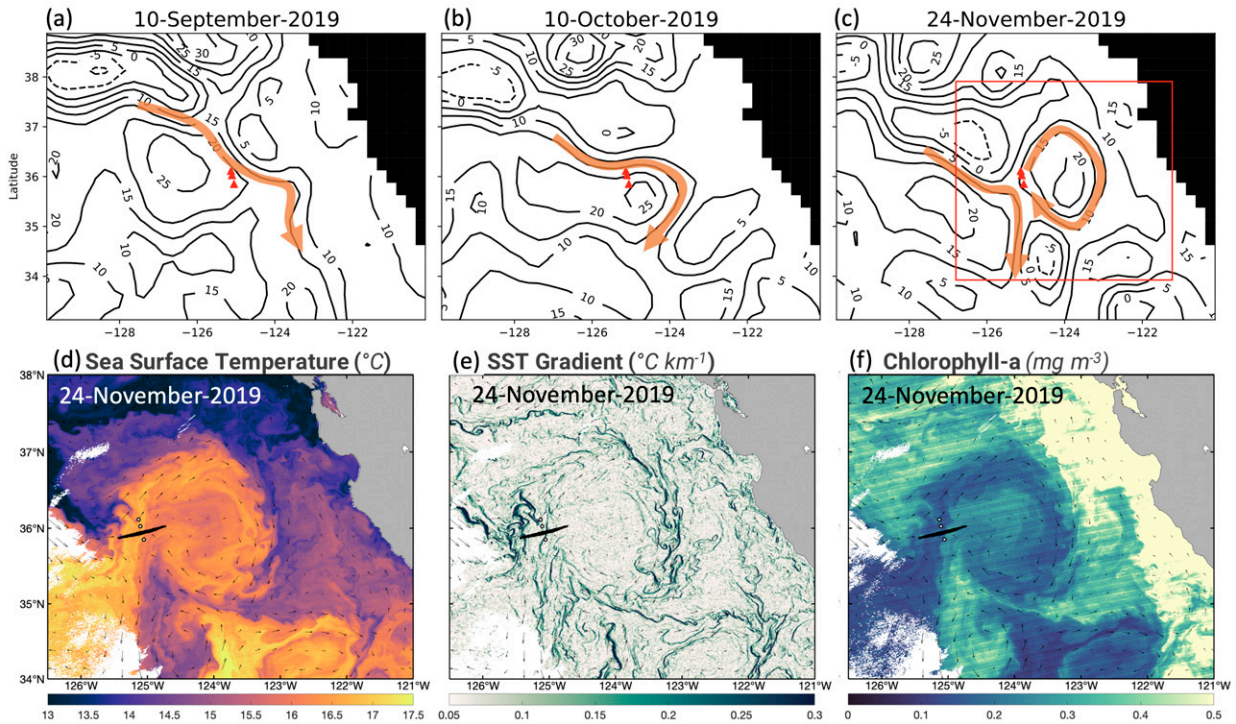


FIG. 5. (a)–(c) The altimetric sea level anomaly (SLA) on 10 Sep, 10 Oct, and 24 Nov 2019 corresponding to the beginning, middle, and end of the campaign, respectively. The thick orange arrows show the pinch-off of mesoscale eddy from the meander of the California current. The three red triangles mark the three mooring locations. The red box in (c) marks the domain boundary for (d)–(f) the SST and surface chlorophyll-a after the eddy formed approximately on 24 Nov (an ascending 750 m resolution swath from VIIRS *Suomi NPP* L2 taken at 2100 UTC). The black lines (60 km long) in (d)–(f) mark the glider flight path.

situ, indicating that the GNSS GPS system is accurate enough to measure the oceanic baroclinic signals.

The difference between the two steric height time series is further binned into different sea states characterized by SWH. As expected, the RMS difference between the two is a function

of sea state (Fig. 7). The RMS difference is about 1 cm for calm seas with SWH < 1 m, 1.7 cm for SWH = 2 m, and 3 cm for SWH > 6 m. These GPS errors may be of large scale and not contribute to 15–150-km-scale errors that are of primary interest here. Detailed discussions are given in section 5.

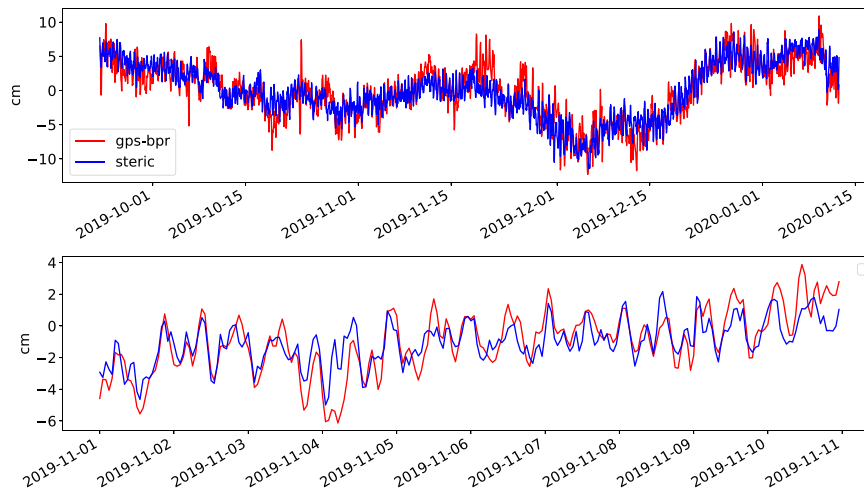


FIG. 6. (top) The steric height from the hydrographic measurements (blue) and the GPS-BPR-derived dynamic SSH. (bottom) As in the top panel, but for a short period (10 days).

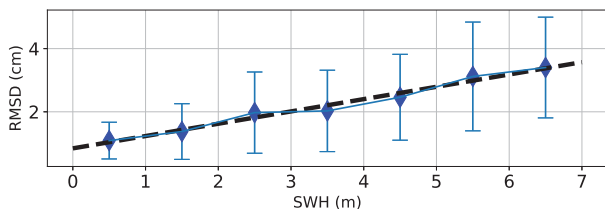


FIG. 7. The RMS difference (RMSD) between the steric heights derived from GPS/BPR and mooring CTDs as a function of significant wave height (SWH). The diamond symbols represent the mean RMSD binned to SWH values with a 1 m bin width. The error bars show the standard deviation of the absolute difference as an uncertainty measure. The line is the linear fit to the mean following  $\text{RMSD} = 0.84 + 0.4\text{SWH}$  (cm).

The difference between GPS-derived and CTD-derived steric height can be scrutinized in frequency space, where we may identify the error sources. The GPS-based and CTD-based steric heights match at low frequencies with equal power spectral density within the 95% uncertainty bounds (Fig. 8). The major difference starts to show for periods less than 10 days, except for several major tidal periods such as  $M_2$  and  $M_4$  where the spectral peaks and coherence are significant. This is visible from the time series in Fig. 6. It is interesting to note that the coherence is high at 7.6-h period, which

corresponding to the frequency of nonlinear interaction between inertial motions and semidiurnal tide denoted  $fM_2$  (Mihaly et al. 1998).

The amplification of the differences over short periods less than 10 days is not fully understood, but could be related to the cadence of weather systems. The largest dispersions are sporadic in time (Fig. 6) and have a linear relationship with sea state (Fig. 7), and could also reflect refraction errors for the GPS systems. Errors in CTD-derived steric height exist but should not be a function of sea state and are less likely to be the dominant error source. The major difference between red and blue lines in Fig. 6 probably arises from the GPS-derived steric heights, which reflect not only GPS errors but also the errors in the IB correction through ERA5 and errors from MSS uncertainties. However, these errors may well be of large spatial scales that are less relevant to the SWOT in situ Cal/Val focus in this region ( $<150$  km; Wang et al. 2018). If the GPS and IB related uncertainty/errors have large spatial scales, they can be removed through a spatial high-pass filter or simply by removing a linear trend along a 150 km distance as done in Wang et al. (2018).

### c. The vertical scale

To minimize the cost of the postlaunch in situ Cal/Val, we may need to tolerate some uncertainties due to missing direct

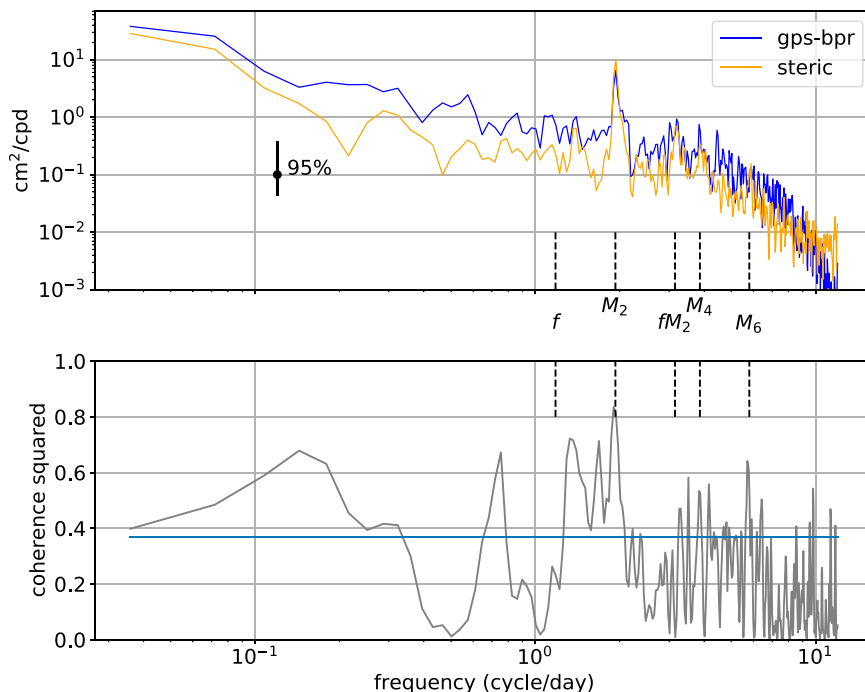


FIG. 8. (top) The frequency spectrum of the full-depth steric height (orange) [right-hand side of Eq. (3)] and the GPS-derived dynamic SSH (blue) [left-hand side of Eq. (3)]. The spectra are calculated using the Welch method with four nonoverlapped segments giving a degree of freedom (DOF) of 8. A Hanning windowing and linear-detrend operation were applied. The 95% significance level with  $\text{DOF} = 8$  is shown by the black vertical bar. (bottom) The magnitude-squared coherence between the two time series using the Welch method with the same number of segments and DOF. The blue horizontal line marks the 95% significant level with  $\text{DOF} = 8$ .

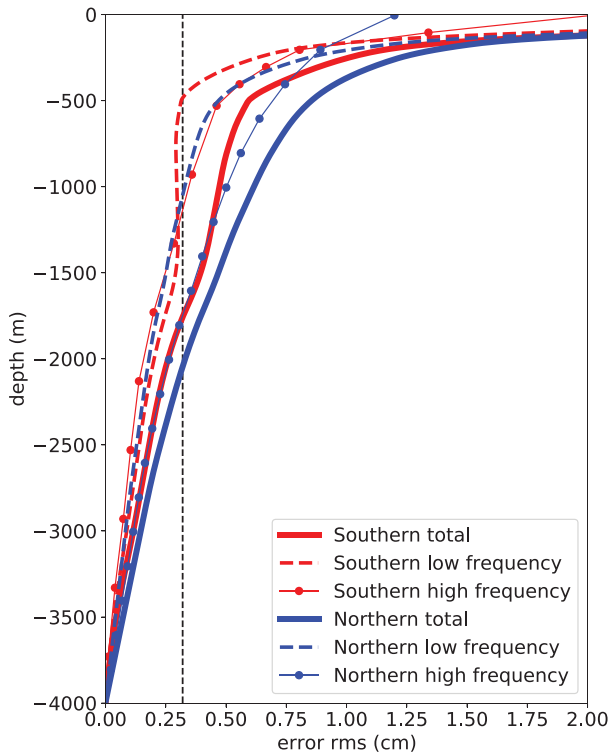


FIG. 9. The RMSE  $\epsilon(z)$  of the upper-ocean steric height relative to full-depth steric height as a function of integration depth. Because the bottom CTD on the northern mooring was corrupted, we chose 4000 m as the deep-ocean reference for both moorings. By definition, the error decreases when the integration depth gets deeper and reaches zero at the bottom (4000 m in this case). The southern mooring is shown in red and the northern mooring in blue. The thick solid lines are for the total signals, the dashed lines for low frequency ( $>48$  h), and the thin solid-dot lines for high frequencies ( $<48$  h). The black dashed vertical line marks the 0.32 cm RMS level, which is derived from  $2 \text{ cm}^2 \text{ cpkm}^{-1}$  wavenumber spectrum noise level for stations separated by 10 km.

measurements of the deep ocean. How deep do we have to measure the ocean to generate a steric height accurate enough for SWOT Cal/Val?

The uncertainty introduced by missing deep-ocean measurement below a depth  $z$  is defined as the steric height integrated between ocean bottom and  $z$ :

$$\eta_{\text{deep}}(z) = - \int_{-H}^z \frac{\rho'(z')}{\rho_{\text{ref}}} dz',$$

where  $\rho'$  is the in situ density anomaly deviation from a time-mean density profile  $\bar{\rho}(z)$ , and  $\rho_{\text{ref}}$  is the mean in situ

density (set to  $1035 \text{ kg m}^{-3}$  here). We quantify the uncertainty using the standard deviation of this deep-ocean steric height  $\epsilon(z) = \text{std}[\eta_{\text{deep}}(z)]$ .

The results based on the northern and southern mooring are shown in Fig. 9. The  $\epsilon(z)$  decreases toward the deeper ocean as defined but with a larger rate in the southern mooring (thick red) than the northern mooring (thick blue). The different vertical scales between the northern and the southern moorings may be caused by different dynamic regimes experienced by the two moorings. The 500 m depth is of particular interest because that is roughly the bottom depth of the Prawler and Wirewalker platform. Table 1 lists some relevant numbers about the errors  $\epsilon(500)$ . The total error  $\epsilon(500)$ , i.e., the error of missing the deep ocean below 500 m, is  $0.61 \pm 0.1$  and  $0.84 \pm 0.17$  cm for the southern and northern mooring, respectively. The errors represent the mean RMS and the standard deviation in a time series of  $\epsilon(500)$  calculated based on segments of a 10-day duration subsampled from either the original or the filtered time series. The error amplitude changes over time. Most of these errors come from high-frequency processes with periods less than 2 days (we will use the format  $T < 2 \text{ d}$  hereafter). They are  $0.51 \pm 0.06$  and  $0.67 \pm 0.14$  cm for the southern and northern moorings, respectively. The low-frequency (2–14 d) component on the other hand has errors less than  $0.15 \pm 0.1$  cm for both moorings, accounting for less than 4% of total variance (Table 1). The deep-ocean ( $<-500$  m) steric height has a 0.5–0.7 cm RMS values and accounts for 5% of the full-depth steric height for high frequencies with periods less than 2 days at the southern mooring. This ratio becomes 30% at the northern mooring. The northern mooring particularly presents a higher deep-ocean high-frequency variability. The causality cannot be confirmed without more independent observations. It may be caused by the topographically generated deep-ocean internal tide/wave signal that is strong for the northern mooring, or simply because of the errors in determining the depths of the deep CTDs, which have large vertical excursions.

The spectrum of the upper-500-m steric height and the full-depth steric height and their coherence are shown in Fig. 10. We used the Welch method with a Hanning window. The full time series is split into nonoverlapping segments. The steric heights of the upper 500 m (blue) and of the full depth (orange) agree well over subinertial frequencies with similar spectra density and high coherence for both moorings. The major difference comes from the superinertial frequencies, especially around the tidal frequencies at  $M_2$  (and  $M_4$  for the southern mooring). The errors are relatively high (green lines) but the coherence (red lines) is still large and significant

TABLE 1. Deep-ocean contribution to steric height  $\epsilon(500 \text{ m})$  for the two moorings at different frequency bands. This represents the error by only measuring the upper 500 m.

	Total RMSE (cm)	2–14-day band (cm)	Variance percentage (2–14 days) (%)	High frequency ( $<2$ days) (cm)	Variance percentage ( $<2$ days) (%)
Southern	$0.61 \pm 0.1$	$0.14 \pm 0.1$	1	$0.51 \pm 0.06$	5
Northern	$0.83 \pm 0.17$	$0.15 \pm 0.07$	3.4	$0.67 \pm 0.14$	31

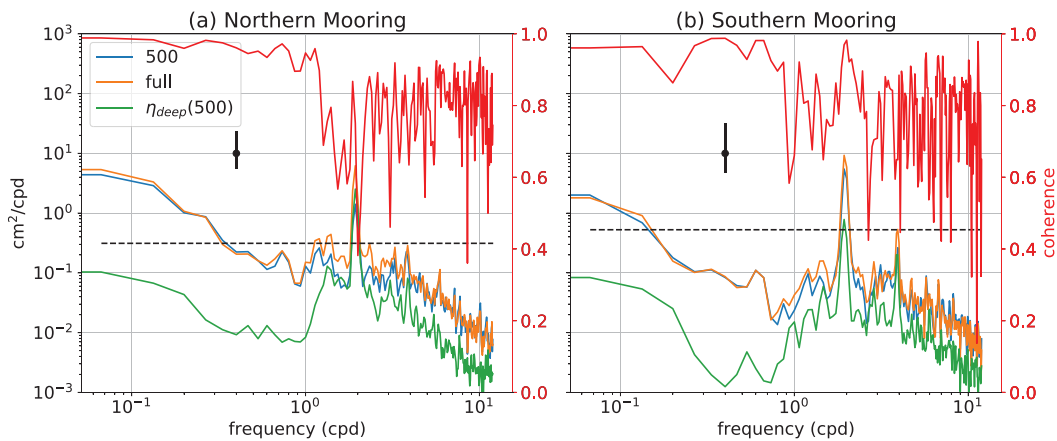


FIG. 10. The frequency spectra of 500 m (blue) and full-depth (orange) steric height and their difference (green) and the magnitude-squared coherence (red). The difference (green) is  $\eta_{\text{deep}}(500)$ . The spectra were calculated using Welch with nonoverlapping segments, each of which is of 15-day duration. The black error bar represents the 95% confidence interval. The degrees of freedom are 10 for the southern mooring and 18 for the northern mooring (due to its longer duration). The 95% significance level of the magnitude-squared coherence is shown by the dashed line: 0.31 and 0.53 for the northern and southern moorings, respectively.

(above 95% confidence level) for both moorings. This reflects that the superinertial motions, especially the semidiurnal internal tides, are of low baroclinic mode and reach deeper in depth than the subinertial submesoscale and mesoscale motions. [see also Lapeyre and Klein (2006) and LaCasce and Mahadevan (2006)].

The errors presented in this section include all spatial and temporal scales. Because of the SWOT focus on scales smaller than the mesoscale, correlated mesoscale scale error among the moorings can be removed, yielding a much smaller residual error budget. The high-frequency deep-ocean steric height with periods less than 2 days has 0.5–0.7 cm RMS and mostly from baroclinic tides (Fig. 10). If only the subinertial motions (2–14-day period) are considered, missing deep ocean introduce less than 2 mm error (Table 1), which is well below the KaRIn measurement error (0.54 cm RMS). These deep-ocean high-frequency signals require deep-reaching mooring CTDs.

#### d. Station-keeping glider as a virtual mooring

Glider, unlike moorings, are mobile and add more flexibility to the campaign. We had one Slocum glider in the 2019/20 campaign for 1) testing the performance of a data assimilation system (Archer et al. 2022) and 2) testing the glider as a virtual mooring for the contingency of a failed mooring.

The glider vertical trajectories generally straight lines underwater, proceeding in a single direction fixed to a magnetic heading. This heading can be chosen to correct for ocean currents if one wishes to hold sampling lines. The downside of a single trajectory underwater means larger errors in station keeping and thus the ability to remain close to a single location. This is because of large distances traversed horizontally underwater, especially while diving deep.

To compensate for this and maintain a fixed position, the glider must have the ability to change heading underwater. It

achieves this by maintaining a course of waypoints underwater which can be in any shape, for instance, a square, triangle, or even back and forth with two waypoints. Built into the underwater positioning is an algorithm to correct for estimated depth averaged current. This allows the underwater vehicle to continuously correct for current and maintain the same positions on Earth underwater for periods of several hours or more.

The Slocum glider's dive speed is about 18–20 cm s<sup>-1</sup> yielding ~45 min per profile for a diving depth of 500 m. This will produce about 30 profiles a day. The capability of a station-keeping glider has been tested in our OSSE study (Wang et al. 2018) and the 2017 field campaign (Clark et al. 2018), where we confirmed that the glider-derived steric height matches the upper-ocean steric height from a nearby mooring for periods longer than 6 h with error-to-signal ratio smaller than 0.5 (figure not shown).

We tested the glider's station keeping again in the 2019/20 campaign and also used the glider as a conduit to connect and test the three moorings. The Slocum glider performed station keeping near the three moorings for three weeks between 27 November and 17 December 2019. The relative location of the glider flight path to three moorings are shown in Fig. 11. The glider stayed for about 3, 5.5, and 6.5 days around the southern, middle, and northern moorings, respectively. The associated mean glider–mooring distances are  $1.2 \pm 0.2$  km,  $0.8 \pm 0.4$  km, and  $0.9 \pm 0.2$  km from south to north. The clusters of the glider surface locations have smaller circles referenced to its own center. The circles have a radius of 233, 350, and 520 m from north to south, respectively. The horizontal spread of the glider surface locations has a comparable size to the watch circle of the southern mooring during this period. A larger spread of the glider paths is expected for a longer duration and/or in a stronger flow field.

The Slocum glider's capability of being a virtual mooring was validated again in this campaign. The RMS difference

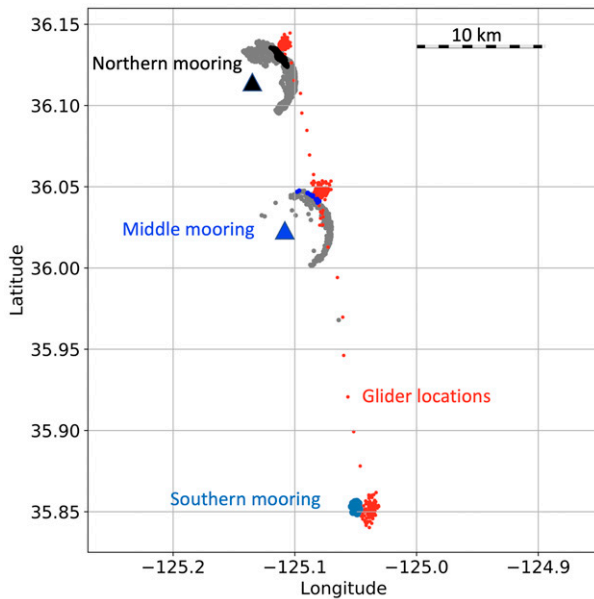


FIG. 11. The locations of the glider (red) and the northern mooring (black), the middle mooring (blue), and the southern mooring (navy blue) during the glider station-keeping phase, 27 Nov–17 Dec 2019. The mean separation distances during station keeping phase are  $0.9 \pm 0.2$ ,  $0.8 \pm 0.4$ , and  $1.2 \pm 0.2$  km for the northern, middle, and southern mooring, respectively. The two triangles show the anchor locations of the middle and northern moorings. The mooring watch circle shown by the gray dots has a radius of 4.5 km.

between glider and mooring upper-ocean (500 m) steric height is about 0.4–0.5 cm. Figure 12 (top panel) shows the time series of the upper-500 m steric height calculated from the glider (blue lines) and the moorings (orange lines). To avoid temporal interpolation errors, we used individual profiles to calculate the steric height without temporal interpolation between the subsurface temperature and salinity profiles. The time associated with the steric height of each profile was taken from the time at 250 m depth.

Figure 12 shows that the upper-500-m steric heights from glider and moorings are closely matched. The RMS differences are 0.4, 0.48, and 0.45 cm for the northern, middle, and southern mooring. The northern mooring has fixed CTDs binned to a 6-min grid close mooring–glider match confirms the capability of gliders to reproduce the upper-500-m steric height to time scales of several cycles per day.

The comparison of the glider to the northern mooring has the least RMS difference. The middle mooring was equipped with a Prawler, similar to a Wirewalker on the southern mooring, but was configured to sample about 8 profiles per day to test the endurance of the mooring. The larger RMS difference is mostly caused by the low temporal resolution (8 profiles per day) in mooring steric height (orange line/symbol in the top-center panel of Fig. 12). Because of the low temporal resolution, the middle mooring undersampled the internal tides especially the peaks that were captured by the glider. For example, the internal tidal variance at the beginning of

12 May 2019 is captured by the glider but not by the mooring (Fig. 12, top-center panel). This indicates the insufficiency of 8 profiles per day sampling frequency.

For the southern mooring comparison (top-right panel), there are superinertial variabilities in the mooring steric height largely captured by the glider except for the tidal peaks on 29 November. The glider dived to 1000 m at this location, so the temporal resolution is half that of the 500 m dives. The resulting lower temporal resolution in the glider steric height introduces an RMS difference 0.45 cm, which is larger than the 0.4 cm at the northern mooring. The time series comparison indicates that mapping the SSH variability due to the internal wave displacement of the density structure of the upper 500 m requires around 24 profiles per day. The spectral and coherence analyses shown in the bottom panel of Fig. 12 confirm the direct visual examination of the steric height time series discussed above. The glider steric height matches the northern mooring steric height in spectral density (bottom left, blue and orange lines) with high coherence ( $>0.6$ ) down to approximately 5–6-h period (bottom left, purple line). For the middle mooring, because of the low temporal resolution in the mooring steric height, the glider–mooring only matches up to the  $M_2$  tidal frequency, so  $\sim 8$  profiles per day can resolve  $M_2$  tides but not superinertial variabilities. For the southern mooring location (bottom-right panel), the mooring and glider match with high coherence ( $>0.6$ ) down to a 6-h period.

In summary, the steric height derived from the glider matched the mooring upper-500-m steric height with 0.4–0.5 cm RMS difference. This largely validated the capability of gliders as a virtual mooring in the Cal/Val region with one caveat that the glider’s error is referenced to the mooring’s upper-ocean steric height, which itself carries about 0.6 cm uncertainty. Even though this uncertainty can be reduced by nearby deep-reaching CTD moorings with instruments in the deep ocean, the added uncertainty should be emphasized in a contingency scenario that a glider is needed to substitute a failed mooring.

#### e. Spatial and temporal variability

Each mooring produces a steric height time series. We can examine the temporal and frequency content of the signal. The spatial–temporal variabilities can be examined by combining the three moorings separated at 10 and 20 km even though a full wavenumber spectrum cannot be calculated across so few mooring separations.

##### 1) TEMPORAL VARIABILITY

In the time domain, the mooring upper-500-m steric height closely follows the gridded SSH over long periods. Figure 13 shows the direct comparison between AVISO and the steric height of the northern and southern moorings (black solid and dashed lines). At the beginning of the campaign in early September 2019, the mooring steric heights and altimetric SSH are all at about approximately 76 cm level. This is associated with a south–north meandering current, whose SSH gradient is largest east–west perpendicular to the mooring array (Fig. 5a). When the meander curved toward the coast to form

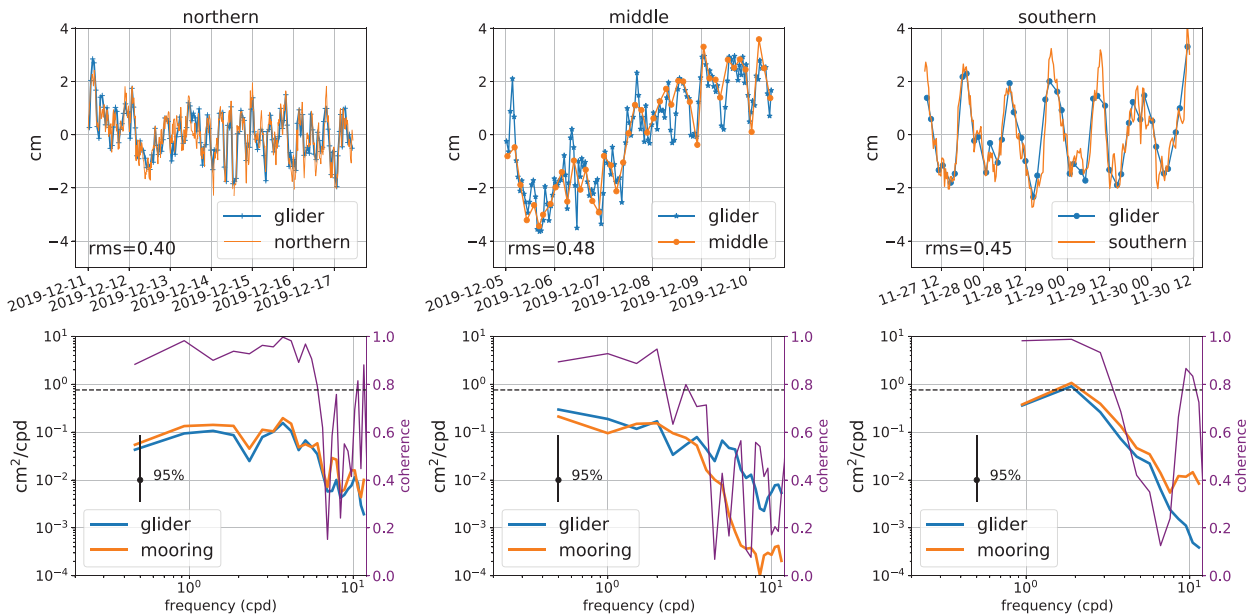


FIG. 12. (top) The upper-500-m steric height reconstructed from the glider (blue lines) and moorings (orange lines). (bottom) The frequency power spectral density for the glider (blue) and moorings (orange). The black vertical lines show the 95% confidence interval with 4 degrees of freedom (three nonoverlapping segments). The magnitude-squared coherence is shown in purple with the y axis on the right and the associated 95% confidence level marked by the dashed lines (left to right) The northern, middle, and southern moorings. The duration of the station-keeping phase was longest at the northern mooring (6.5 days) and shortest at the southern mooring (3.5 days).

an isolated mesoscale eddy during the eddy formation, the flow turned zonal (Fig. 5b) and the SSH differences between the three moorings can be as large as 10 cm between the southern and northern moorings, for example, at the end of October 2019 (Fig. 13, top panel). Near the end of November 2019, when the eddy was finally formed and detached (Fig. 5c), the meander regained its original north–south orientation with isolines oriented along the direction of the mooring array, resulting in a minimal SSH difference among the moorings. This eddy development can be seen from both altimetric SSH and mooring steric height, but the two-dimensional altimetric SSH field reveals more of the physical process than the one-dimensional array.

The gridded altimetry product and mooring have high coherence ( $>0.6$ ) for periods longer than 20 days (figure not shown). The match between altimetric SSH and mooring upper-500-m steric height with less than 2 cm RMS error validates the upper-500-m steric height in representing satellite SSH over low frequencies. For periods shorter than  $\sim 20$  days, the mooring steric height exhibits more variability than the gridded altimetric product, which is expected. From the example shown in the bottom panel of Fig. 13, the  $M_2$  tide can be coherent and propagate from north to south shown by the gray arrow, but the coherency among the three moorings is intermittent. Over a 2-day period between 11 and 13 November, for example, the  $M_2$  tidal peaks are less obvious at the northern mooring than at the southern mooring (Fig. 13, bottom panel).

The southern and northern mooring time series (Fig. 13, upper panel) reveal that the  $M_2$  tide is stronger and more coherent at the southern mooring than the northern mooring.

From a tidal analysis on the two steric height time series (figure not shown), the southern mooring has an  $M_2$  steric height amplitude of 1.7 cm while the northern one has an amplitude of 0.7 cm. The  $M_2$  baroclinic tide represented by the steric height is dominated by the first baroclinic mode that has a large wavelength longer than 100 km.

To address the question of why the  $M_2$  tide is so different between two moorings separated by 30 km, we first eliminated the possibility that the difference comes from different mooring designs. The southern mooring uses a subsurface taut mooring connected to the profiler and surface buoy above by a reserve catenary. This design has a much smaller watch circle (250 m radius) than the northern slackline design mooring ( $\sim 4$  km radius). However, it is unlikely that this contributes to the difference in the  $M_2$  signal at the different moorings, based on the glider results during its station-keeping phases shown in Fig. 12. The time variability at the  $M_2$  tidal period is well characterized by the glider for both the southern and the northern moorings. During the 6-day period where the glider operated near the northern mooring, it confirmed the weak  $M_2$  signal there. Likewise, at the southern mooring, the glider confirmed the elevated  $M_2$  variability in steric height there. This mooring–glider comparison largely eliminates the influence of mooring design on the reconstruction of the coherent tides. As a result, the significantly different  $M_2$  tide between the northern and the southern moorings appears to be real.

One possibility for the different tides between the northern and the southern moorings is that this small-scale difference is expected due to multiwave interference that has been

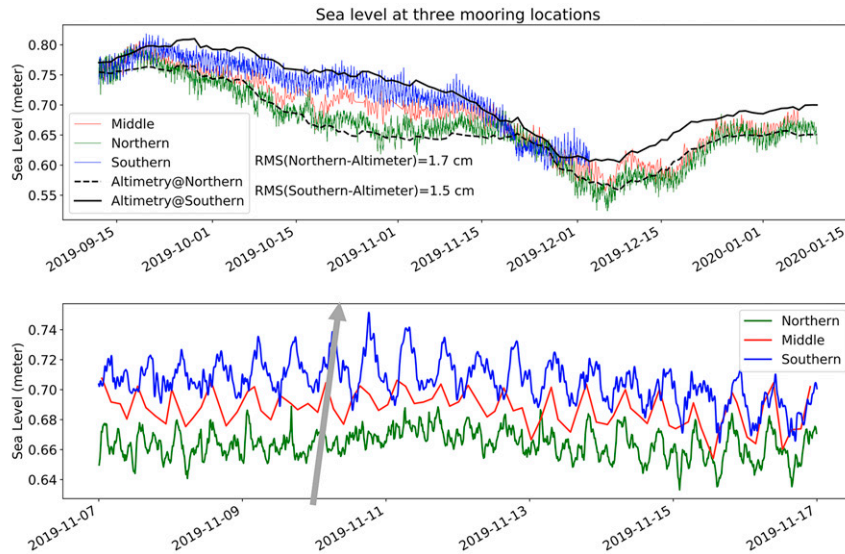


FIG. 13. (top) The time series of the upper-500-m steric height from three moorings (colored lines) offset by a constant 496.91 m, and the altimetric sea level anomaly interpolated at northern mooring (black solid) and southern mooring (black dashed). The RMS differences between WHOI mooring and SIO mooring steric height from their local altimetric sea level anomaly is 1.7 and 1.5 cm, respectively. (bottom) The same mooring steric height time series, but focusing on a 10-day window between 7 and 17 Nov 2019. The semitransparent gray arrow marked the propagation of the internal tides from the northern mooring through the middle mooring and to the southern mooring.

observed in the conventional altimetry (Zhao et al. 2019; Zaron 2019). An altimetry-based internal tide model that fits plane internal waves with multiple directions does also show similar amplitude variation of the mode-1  $M_2$  internal tide over the 30 km distance between the two moorings (Zaron 2019).

Another possibility is the modulation of coherent tides by balanced motions (e.g., Ponte and Klein 2015). The mesoscale and smaller mesoscale eddies are stronger at the northern mooring location than the southern mooring location, resulting in stronger eddy modulation of the tides and reduced tidal coherency. This can be seen from the frequency spectra of the steric height field of the three moorings (Fig. 14). The stronger  $M_2$  tides at the southern mooring discussed above are illustrated in the frequency spectrum, i.e., the green line is much higher than the blue line at the  $M_2$  frequency. The three moorings have matched energy on the low-frequency end with periods longer than 20 days. However, the spectral energy level at the southern mooring is drastically different from and one order of magnitude weaker than the other two moorings over 1–10-day periods. The gridded altimetry SSH maps (Fig. 5) show that the southern mooring is on the warm side of the meander and inside of the mature eddy at later stage, while the northern mooring spent more time on the further edge of the eddy where sharp horizontal fronts can be more prominent. This is confirmed by the horizontal gradient of SST, which is persistently stronger at the northern mooring location than at the southern mooring (figure not shown). This set of evidence points to the hypothesis that mesoscale eddies can

modulate coherent low mode tides within a distance shorter than the tidal wavelength. The 2D SSH field to be observed by SWOT can be very useful to detect these small-scale eddy-wave interactions. Further proof of the hypothesis needs more observations or process-oriented numerical modeling studies and will be pursued elsewhere.

## 2) SPATIAL VARIABILITY

With two full-depth moorings at the northern and southern locations, we can start to examine the spatial variability from

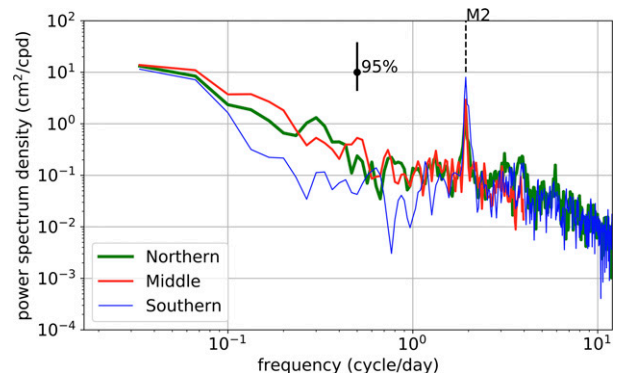


FIG. 14. The frequency spectra of the upper-500-m steric height from the northern (blue), middle (red), and the southern mooring (green).  $M_2$  tidal frequency is marked by the dashed vertical line. The middle mooring spectrum (red) was cut at 4 cycles per day for its limited sampling frequency at 8 profiles per day.

TABLE 2. RMS differences between the northern and the southern moorings for the period 10 Sep–25 Nov 2019 when full-depth measurements are available at both sites. The temporal-scale separation is done in frequency space through Fourier analysis without windowing. The bottom row is done through a three-mooring scale separation described in the text representing a back-of-envelope calculation of the small-scale ( $< \sim 30$  km) variability. The unit for all values is cm.

	Full water column	0–500 m	500–4000 m
All frequencies	3.2	2.8	0.9
<14 days	1.6	1.4	0.8
2–14 days	0.7	0.7	0.2
<2 days	1.5	1.2	0.7
Anomalies to a linear function of the three moorings		0.2–0.7	

the mooring difference. Table 2 shows that the RMS difference over 30 km is 3.5 cm based on the full-depth steric height, among which 2.8 cm is due to the upper 500 m and 1 cm to the deeper ocean. These values include the influence of the wavelengths longer than 150 km, which is beyond the focus of the in situ Cal/Val. With only three moorings spanning 30 km, it is impossible to single out the signals with wavelength less than 150 km, but in general longer wavelengths are associated with longer periods. For example, these RMS differences are reduced for periods less than 14 days and significantly reduced for the 2–14-day band. The variability with periods less than 14 days is dominated by high frequencies ( $> 1/2$  cycle day $^{-1}$ ). This dependence of RMS difference on time scales is expected for a typical SSH frequency spectrum that is dominated by low-frequency (monthly and longer) variabilities and tidal peaks over high (superinertial) frequencies (e.g., Fig. 14).

The middle mooring does not have deep CTDs below the Prawler and samples only the upper 500 m. If we only focus on the upper-500-m steric height, the three moorings can be used to derive steric height difference for separation distances of 10 and 20 km. The standard deviations of the differences are 1.6 and 2.0 cm for 10 and 20 km, respectively.

These analyses with a single mooring (section 4c, Table 1) or two-mooring differences (Table 2) cannot distinguish different spatial scales, but we have used the above frequency filtering to isolate motions on SWOT spatial scales and thus could estimate the expected RMS differences due to these motions on the single spatial lag of 30 km. This is the size of SSH differences expected due to motions of interest to SWOT over such distances. In addition, with three moorings, we can begin to decipher the spatial–temporal variabilities due to the smallest-scale motions, even without the actual wavenumber spectrum. The main technique is discussed as follows.

Given three moorings with separation distances of 10 and 20 km, we have three points spanning 30 km distance. To examine small-scale signals, we removed the large-scale influence by removing a spatial linear trend through the three moorings for each hourly snapshot as shown in

the schematic diagram in Fig. 15a. The middle mooring time series is linearly interpolated from 8 profiles per day to hourly, which inevitably introduces errors. The deviations from the fitted linear trend are considered the SSH anomaly at small scales.

The linear-trend removal is a crude spatial high-pass filter. The effectiveness of removing the local linear trend is evaluated using a Monte Carlo simulation to test a Hanning high-pass filter with different window sizes. We first generate 5000 128-km-long synthetic SSH profiles with certain wavenumber spectral slopes, then sample the profiles in the middle at three locations separated by 10 and 20 km, resembling the prelaunch campaign mooring placement. The synthetic mooring data are separated into large scale and small scale using the same method of fitting a three-point linear trend. The results are compared with results produced by a high-pass Hanning filter of different window widths. We find that for synthetic SSH profiles with  $k^{-4}$  wavenumber spectrum, the smallest difference between removing a local linear trend of the three moorings and a Hanning-window filtering occurs at 22 km Hanning-window width. For  $k^{-2}$  profiles, it is at 32 km. The SSH profile is “smoother” for steeper wavenumber spectrum, e.g.,  $k^{-4}$ , so the local linear trend captures and removes large-scale signals more effectively. The anomalies after removing the local linear trend are mostly from spatial scales less than approximately 30 km. We denote these anomalies as “small scale” and the linear trend as “large scale” in the following paragraph. It is worth emphasizing again that this operation is a crude way of separating small and large scales, given the limitation of the spatial coverage of the data.

The derived small-scale variability is significantly weaker than the large-scale variability (Fig. 15b). The RMS values of the total upper-500-m steric height for the three moorings are 1.9, 1.3, and 1.9 cm from north to south. The corresponding large scales defined by the linear trend have RMS values of 1.7, 1.2, and 1.9 cm. The small-scale ( $< \sim 30$  km) steric height is 0.4, 0.7, 0.2 cm for the northern, middle, and southern moorings, respectively. These values for small scales are smaller or close to the SWOT KaRIn noise values around 0.54 cm (section 2d). It indicates that the SSH signal at the Cal/Val site can be weaker than the SWOT KaRIn noise for spatial scales 20–30 km and smaller. This result is consistent with Wang et al. (2019).

Note that the sum of small-scale and large-scale temporal variances is larger than the variance of the total signal. This provides evidence that this spatial filtering does not separate the signal in the temporal space. However, removing the local linear trend effectively removes most of the low-frequency variability that is visually obvious in the time series (Fig. 15b) and also clearly shown in the frequency spectra in Fig. 15c, where the power spectra of the total and large-scale signals converge over periods longer than 10 days (blue and orange lines). Removing the linear trend also effectively removes most of the  $M_2$  baroclinic tides in the steric height, which means that the baroclinic tides have spatial scales larger than about 30 km. Even though the large-scale signal is more energetic than the smaller spatial signal over almost all

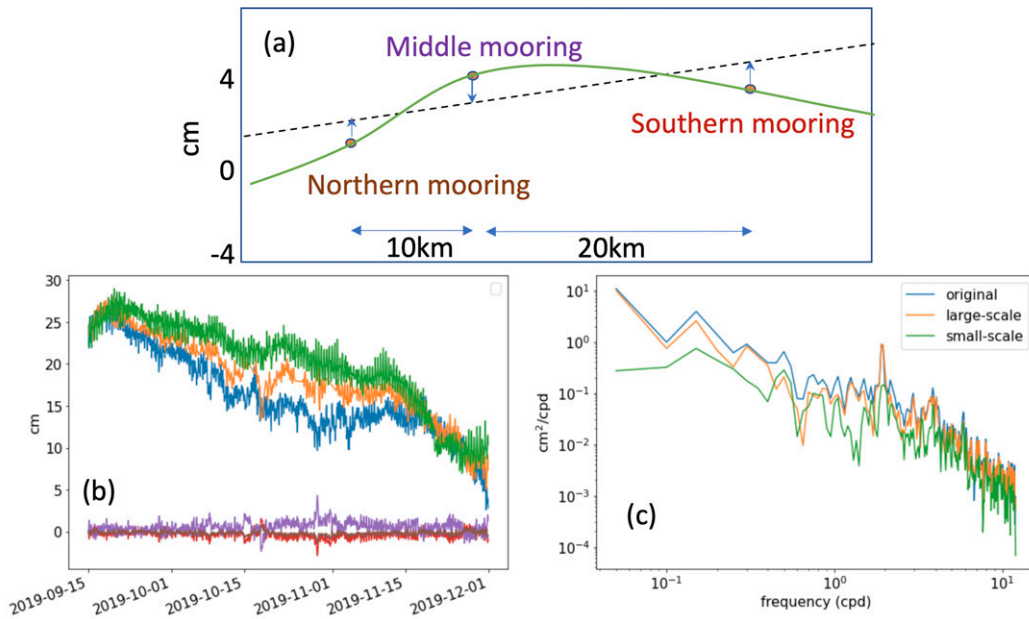


FIG. 15. (a) The schematic of deriving small-scale anomalies from three moorings. The linear trend (dashed line) was derived through the least squares method. The deviation of each mooring steric height from their linear trend is denoted as the small-scale component. Removing the linear trend over a 30 km segment is similar to high-pass filtering with a 20–30-km-wide Hanning window depending on the wavenumber slope of the signal. (b) The original steric height of each mooring (green, orange, and blue lines). The small-mesoscale signals defined in (a) are shown by purple, red, and brown lines for the three moorings. (c) The frequency spectra for the original steric height (blue), the linear trend representing the large-scale (orange), and the small-scale steric height (green) averaged over the spectra of the three moorings.

frequencies, the small-scale signal is particularly large over the period range of 2–5 days relative to the large scale. With a caveat of uncertain significance, we may tentatively associate <30 km spatial scales with 2–5-day temporal scales. This spatial–temporal-scale association may have a practical value for designing the optimal error covariance matrices in the data assimilation system with the multiscale approach, such as Li et al. (2019), D’Addezio et al. (2019), and Archer et al. (2022).

#### f. Comparison to Sentinel-3A SSH

The *Sentinel-3A* ground track was not a factor for the design of the SWOT Cal/Val orbit. It is rather fortunate that one of the *Sentinel-3A* (*S3A*) ground tracks is in the middle of a SWOT swath along the fast-repeating orbit. For this reason, the mooring array in the prelaunch field campaign was placed along the *S3A* ground track (Fig. 2). During the 2019/20 campaign period, *S3A* passed the mooring array five times (Fig. 16). The mooring steric heights (upper 500 m) match the *S3A* measurements within 2 cm RMS. There were two times when the steric heights and *S3A* values were different (the third and fifth rows). Despite the sizeable differences, the spatial structures in the mooring array steric heights resemble the spatial structures of the *S3A* SSH profiles. However, bias corrections of 2 and 6 cm were applied to 6 November 2019 and 2 January 2020 profiles, respectively. The nature of the bias is

unknown at the time of writing and deferred to future investigations.

#### g. Bottom pressure

Bottom pressure recorders measure both the barotropic (due to additional water mass above the BPR) and baroclinic (due to interior temperature/salinity changes) signals on the ocean floor. The BPRs deployed in this campaign have enough precision to detect millimeter-level signals, but BPRs suffer from a large long-term drift that may be mistaken for a low-frequency signal in our ~90-day records. Ray (2013) analyzed a network of BPRs of this type, showing that the BPR-derived tide matches the altimetric tide model with about 5 mm RMS difference for the  $M_2$  constituent. The BPRs used in the campaign should be accurate enough to detect deep baroclinic pressure signals even though separating them from much more energetic barotropic tides based on a single mooring is impossible (Ray 2013). The most prominent signal in the bottom pressure is the tide (Fig. 17a). We fit 53 tidal constituents to the measured bottom-pressure signal to produce a detided bottom pressure record (Fig. 17b) using the same tool from Ray (2013). The detided signals are relatively small (2.3–2.6 cm), but still potentially important. Unfortunately, we have little information about the spatial scale of the signals contributing to these residual bottom pressure signals. Taking the difference between the two detided bottom-pressure records can give us a vague sense of how small-scale signals

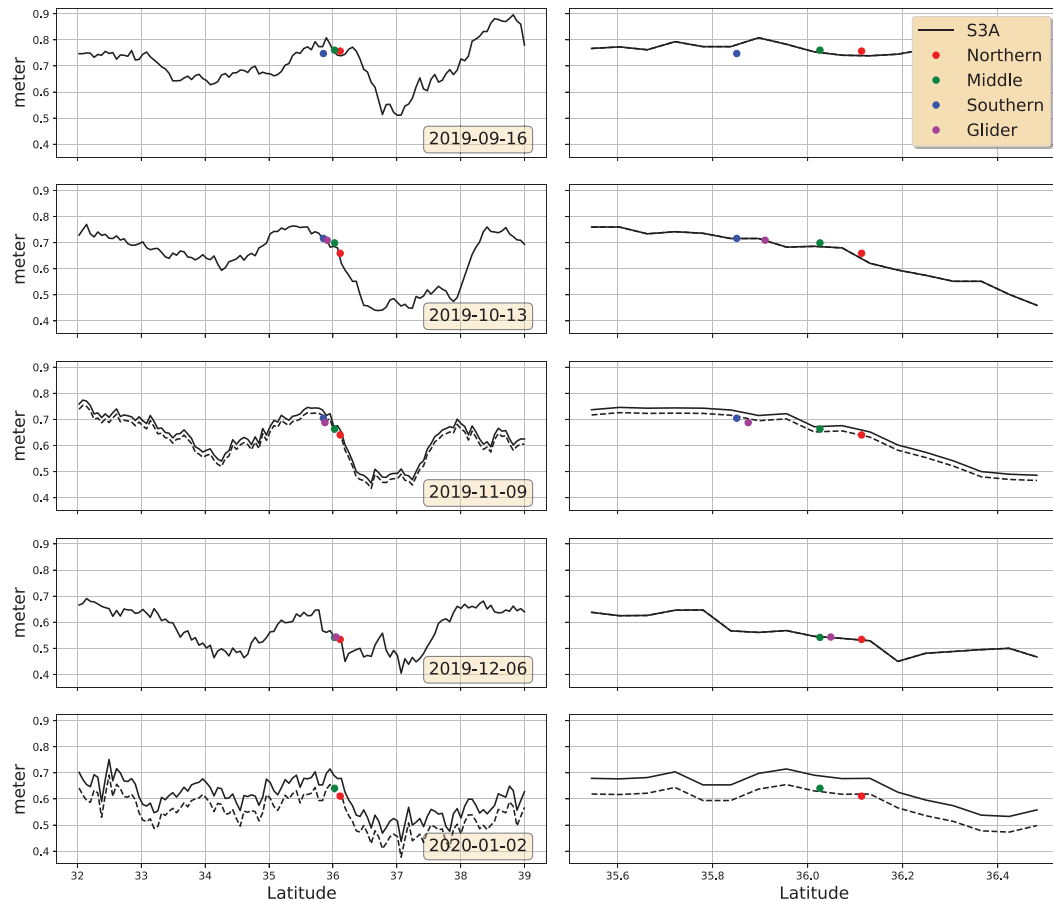


FIG. 16. The five *Sentinel-3A* SSH profiles during the 2019/20 campaign period that pass the mooring array (black lines). They are the L3 product with ocean (barotropic) tides, dynamic atmosphere correction (DAC), and long-wavelength-error (LWE) correction applied. The colored dots show the upper-500-m steric height from the northern (red), middle (green), and southern (blue) moorings and the glider (purple). (left) The 7° segment to show the large-scale context. (right) The same profile, but zooming in to focus on the mooring array within 100-km-wide segments. The dashed lines in the third and fifth rows are the black lines offset by 2 and 6 cm, respectively. The steric height is calculated from the original in situ density without removing the time mean, then offset by 496.385 m to match the *Sentinel-3A* profiles.

might contribute. This difference has an RMS amplitude of 0.6 cm based on the period of 1 October 2019–1 October 2020 when the bottom pressure drift becomes less obvious. It contains both barotropic and baroclinic signals, including several tidal frequencies and low-frequency variability, and the parabolic shape of the difference curve (Fig. 17b) suggests it may also be affected by differences in the low-frequency drift of the two bottom pressure recorders. Removing a quadratic fit to the difference between the two detided bottom-pressure records reduces the RMS difference to about 0.4 cm, which is below the SWOT KaRIn noise level derived in section 2d.

### 5. The design of a SWOT postlaunch campaign

The main purpose of the SWOT prelaunch campaign described in the paper is to provide information for the design of an effective yet affordable postlaunch SWOT ocean in situ observing system for the mission's calibration and validation.

To validate the SWOT SSH, we need an array of observations for comparison with the nearly simultaneous measurement taken by the satellite in less than 23 s over 150 km. The resolution of SWOT in the California Cal/Val region is about 20 km in wavelength, below which the baroclinic SSH becomes less than KaRIn instrument noise (Wang et al. 2019). To meet the Nyquist wavelength requirement of 20 km, we need a measurement every 10 km. Although Wang and Fu (2019) indicated that the onboard nadir altimeter is able to validate SWOT at wavelengths longer than 120 km, we feel that, in order to reduce cost, it is acceptable to deploy an array of 11 moorings covering 100 km to meet the in situ Cal/Val objectives.

Based on the analysis presented in the paper, it is acceptable to sample only the upper 500 m for the low-frequency ocean variability. However, it is desirable to sample the ocean deeper than 500 m to capture the deep signals of internal tides and occasional deep eddies. Since the wavelengths of internal

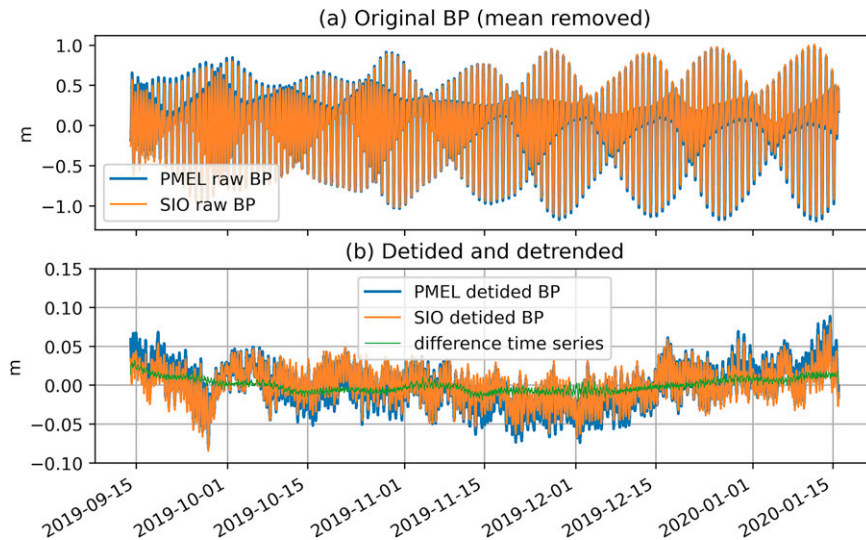


FIG. 17. (a) The original time series of the bottom pressure from the southern (orange) and the northern (blue) BPRs. (b) The residual after removing the fitted tides and linear trends. We fit 53 tidal constituents to the 4-month-long time series to reduce the residual. The remaining signal of each BPR still has 2.2–2.4 cm standard deviation.

tides are longer than 60 km (the two lowest modes of the  $M_2$  tides; Zhao et al. 2019), the required Nyquist sampling interval for low-mode internal tides is 30 km. Shown in Fig. 18 is a baseline design of the postlaunch observing system. It contains 11 moorings with 4 of them (triangles) consisting of a Wirewalker and deep CTDs like the SIO system. The remaining 7 moorings are Prowler moorings like the PMEL system, sampling only the upper 500 m. These instruments will provide time series observations that allow the construction of the snapshots of steric height for comparison with the SWOT SSH measurement on a daily basis. The difference between the two observations will provide an assessment of the SWOT measurement errors for the small-wavelength range reconstructed by the in situ mooring array (20–100 km). Its wavenumber spectrum will be compared with the SWOT requirement (Fig. 1).

Based on the results from the prelaunch campaign, GPS buoys and BPRs are not critical for meeting the Cal/Val objectives. To make accurate IB correction for the SWOT SSH, one barometer at the center of the array is included in the design.

Two gliders are included to sample the cross-track ocean variability to aid the estimation of the two-dimensional state of the upper ocean for validating the science goals of the mission to determine the circulation of the upper ocean. If funding permits, more gliders would be highly desirable for achieving the science goals. As illustrated in the paper, the gliders, when operating in the station-keeping mode, will also serve as a contingency for any failed mooring.

Given the constraints of the mission's budget, this design presents a minimum system for meeting the mission's Cal/Val objectives. We look forward to opportunities of collaboration with other interested parties to expand this SWOT Cal/Val

array into a larger-scale, submesoscale-focused experiment in this region.

## 6. Discussion and conclusions

It has been shown that observations from the moorings and the glider can be used to reconstruct a steric height field with accuracy at an RMS error below 1 cm at each location level. There are, however, remaining uncertainties in the accuracy of the horizontal wavenumber spectrum produced by an array of these moorings.

The moorings' large watch circles might be a source of uncertainty in making an SSH wavenumber calculation for the SWOT Cal/Val purpose. The watch circle can reach a 4 km radius. It may change the spacing between moorings and result in nonuniformly spaced mooring array. In addition, the deviation from the centerline of the mooring array (the middle of the SWOT swath) can also be as large as the watch circle radius. These along-track and cross-track drifts of the moorings will introduce errors and uncertainties, but we do not have a formal assessment of the error in this study. In any case, the size of the watch circle is less than the 15–20-km-wavelength resolution of SWOT in the Cal/Val region (Wang et al. 2019).

The deep-ocean steric height has variability and can contribute to the overall steric height signal. Based on the ~90 days of mooring observations collected during the 2019/20 campaign, the consequence of missing the deep-ocean steric height was about 0.6–0.8 cm standard deviation for each mooring, mostly arising from baroclinic tides (Fig. 10).

There is some evidence that eddies at and below 500 m occasionally occur in the Cal/Val region (Collins et al. 2013). Although Collins et al. (2013) do not report on the water

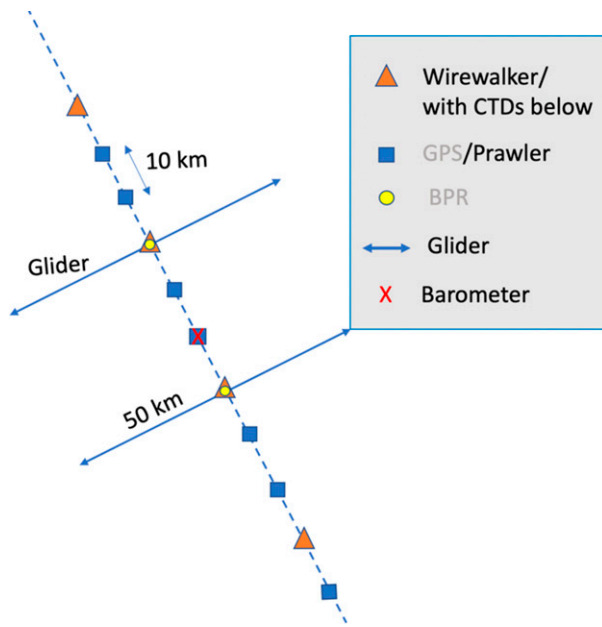


FIG. 18. A minimum baseline for the SWOT postlaunch ocean Cal/Val field campaign. The four hybrid moorings with full-depth  $T/S$  measurements can capture deep-reaching baroclinic tides with relatively longer wavelengths. The seven Prawlers will measure the upper-500-m steric height. Two gliders will sample the cross-swath direction and also serve as a contingency for failed moorings. The barometer will provide high-precision, high-frequency atmospheric pressure for IB correction. BPRs and GPS receivers are not part of the minimum baseline but will be a valuable upgrade.

column structure associated with the observed deep eddies, they could contribute to variability in steric height and to significant nonzero velocities at 500 m depth. For example, assuming a mode-1 structure, a 25-km-wide eddy at 1500 m with  $\sim 10 \text{ cm s}^{-1}$  velocities as reported by Collins et al. (2013) would be associated with a  $\sim 1 \text{ cm}$  change in steric height across its diameter. They also observed an eddy at 660 m depth with velocities that would correspond to 1.4 cm steric height signal across the eddy with a diameter of 54 km at that depth. However, deep eddies need not be associated with a mode-1 structure. For example, Gula et al. (2019) report on the presence of deep submesoscale coherent vortices (SCVs) in the Gulf Stream with diameters of 10–30 km. Those SCVs have a mode-2 like signature that would have little if any impact on steric height (e.g., Fig. 2d in Gula et al. 2019). Given the potential for deep eddies to contribute a small amount of steric height variability, a subset of moorings in the SWOT Cal/Val effort will monitor the deep ocean to account for these signals if they arise (Fig. 18).

Even though the error in GPS SSH from a single buoy ( $>1 \text{ cm RMS}$ ) is larger than SWOT mission requirements, much of this error is attributed to sea-state and water-line errors, and intrinsic GPS errors (e.g., from tropospheric refraction) that are spatially correlated over the campaign footprint. Significant cancellation of common mode errors can thus be expected from combined processing of observations

of multiple buoys operating in the same campaign theater. This is supported by recent tandem buoy campaigns in the Bass Strait (Zhou et al. 2020) and near the Harvest platform (Haines et al. 2019), both of which suggest that errors (on  $\Delta\text{SSH}$  between buoys in proximity) are reduced to less than 1 cm. Whether the accuracies achieved can approach the stringent requirements imposed by the validation of the SWOT wavenumber spectrum remains an open question (Zhou et al. 2020). Regardless, the GPS buoy technique has advanced significantly and already offers a powerful means of resolving discrepancies between steric height (as measured with hydrographic techniques) and geodetic SSH (as measured by SWOT).

We have shown that it is possible to measure the steric contribution to sea surface height to  $<1 \text{ cm RMS}$  precision with several moorings and a glider. This allows confidence that an array of moorings and collocated glider lines (e.g., Fig. 18) will allow for a robust oceanographic calibration and validation of the KaRIn sensor on board the SWOT satellite during the planned 1-day fast-repeat period before the satellite is moved to its final orbit.

This is the first time when a combination of independent high-precision in situ instruments is used to analyze the SSH budget focusing on such small spatial scales (less than 30 km) and high frequencies (period less than monthly). The results shed light on the design of the SWOT postlaunch field campaign as well as the ocean physics over such small scales and high frequencies (periods ranging from hours to months).

We have shown that the ocean sea surface height measured by GPS, which is like altimeter/SWOT measurements, matches the steric height derived from the temperature and salinity measurements using CTDs after subtracting the bottom pressure and applying the inverted barometer correction. The consistency between the GPS-BPR and the mooring steric height validated the utility of the steric height as the ground truth for satellite calibration and validation. Even though the absolute RMS difference between GPS-BPR-derived steric height and CTD-derived steric height is larger than 1 cm, how much of the error is due to the large-scale common mode GPS error is unknown, but expected to be largely removable. The utility of GPS in the SWOT Cal/Val is still under investigation through the second GPS on the middle mooring. The major advantage of using steric height is the absence of the errors due to surface waves.

The variability in steric height is mostly due to the upper-ocean processes. For example, the deep-ocean ( $z < -500 \text{ m}$ ) steric height variability has a standard deviation of 0.6–0.8 cm, most of which comes from superinertial frequencies, especially around the semidiurnal  $M_2$ . If only subinertial variabilities with periods between 2 and 14 days are considered, missing deep ocean results in  $<2 \text{ mm}$  uncertainty.

Small scales less than 30 km wavelength have very weak steric height variation, 0.2–0.7 cm standard deviation near the SWOT Cal/Val campaign region diagnosed from the 2019/20 campaign conducted in the wintertime. This small-scale variability is estimated based on the deviations of the three mooring steric heights from their spatial linear trend. This weak small-scale steric height signal underlines the challenge for

SWOT, but also highlights the opportunities provided by SWOT and the values of a full-scale array with a dozen CTD moorings in conducting the mission Cal/Val and studying the small-scale ocean circulation.

*Acknowledgments.* We are grateful to Anna Savage and R/V *Sally Ride* captain and crew for the unplanned recovery of the Wirewalker, and to Hong Zhang for providing ERA5 atmospheric pressure for the IB correction, Ed Zaron for the discussion on internal tides, and Marie Eble and George Mungov for the discussions on the tidal reconstruction from BP. The research was carried out at the Jet Propulsion Laboratory, California Institute of Technology, under a contract with the National Aeronautics and Space Administration (80NM0018D0004). All authors are supported by the SWOT project. J. T. Farrar was partially supported by NASA NNX16AH76G. The in-situ observations are available for download at <https://podaac.jpl.nasa.gov/>.

## REFERENCES

- Archer, M. R., Z. Li, J. Wang, and L.-L. Fu, 2022: Reconstructing fine-scale ocean variability via data assimilation of the SWOT pre-launch in situ observing system. *J. Geophys. Res. Oceans*, **127**, e2021JC017362, <https://doi.org/10.1029/2021JC017362>.
- Bertiger, W., and Coauthors, 2010: Single receiver phase ambiguity resolution with GPS data. *J. Geod.*, **84**, 327–337, <https://doi.org/10.1007/s00190-010-0371-9>.
- , and Coauthors, 2020: GipsyX/RTGx: A new tool set for space geodetic operations and research. *Adv. Space Res.*, **66**, 469–489, <https://doi.org/10.1016/j.asr.2020.04.015>.
- Bonnefond, P., and Coauthors, 2019: Corsica: A 20-yr multi-mission absolute altimeter calibration site. *Adv. Space Res.*, **68**, 1171–1186, <https://doi.org/10.1016/j.asr.2019.09.049>.
- Callies, J., and W. Wu, 2019: Some expectations for submesoscale sea surface height variance spectra. *J. Phys. Oceanogr.*, **49**, 2271–2289, <https://doi.org/10.1175/JPO-D-18-0272.1>.
- Capet, X., J. C. McWilliams, M. J. Molemaker, and A. F. Shchepetkin, 2008a: Mesoscale to submesoscale transition in the California Current system. Part I: Flow structure, eddy flux, and observational tests. *J. Phys. Oceanogr.*, **38**, 29–43, <https://doi.org/10.1175/2007JPO3671.1>.
- , —, —, and —, 2008b: Mesoscale to submesoscale transition in the California Current system. Part III: Energy balance and flux. *J. Phys. Oceanogr.*, **38**, 2256–2269, <https://doi.org/10.1175/2008JPO3810.1>.
- Chereskin, T. K., C. B. Rocha, S. T. Gille, D. Menemenlis, and M. Passaro, 2019: Characterizing the transition from balanced to unbalanced motions in the Southern California Current. *J. Geophys. Res. Oceans*, **124**, 2088–2109, <https://doi.org/10.1029/2018JC014583>.
- Clark, E. B., and Coauthors, 2018: Station-keeping underwater gliders using a predictive ocean circulation model and applications to SWOT calibration and validation. *IEEE J. Oceanic Eng.*, **45**, 371–384, <https://doi.org/10.1109/JOE.2018.2886092>.
- Collins, C. A., T. Margolina, T. A. Rago, and L. Ivanov, 2013: Looping RAFOS floats in the California Current system. *Deep Sea Res. II*, **85**, 42–61, <https://doi.org/10.1016/j.dsr2.2012.07.027>.
- Copernicus Climate Change Service, 2017: ERA5: Fifth generation of ECMWF atmospheric reanalyses of the global climate. Copernicus Climate Change Service Climate Data Store, accessed 1 March 2020, <https://cds.climate.copernicus.eu/cdsapp#!/home>.
- D’Addezio, J. M., S. Smith, G. A. Jacobs, R. Helber, C. Rowley, I. Souopgui, and M. J. Carrier, 2019: Quantifying wavelengths constrained by simulated SWOT observations in a submesoscale resolving ocean analysis/forecasting system. *Ocean Modell.*, **135**, 40–55, <https://doi.org/10.1016/j.oceanmod.2019.02.001>.
- Desai, S., and Coauthors, 2018: Surface Water and Ocean Topography Mission (SWOT) project science requirements document. Jet Propulsion Laboratory Doc. JPL D-61923, revision B, 29 pp.
- d’Ovidio, F., and Coauthors, 2019: Frontiers in fine-scale in situ studies: Opportunities during the SWOT fast sampling phase. *Front. Mar. Sci.*, **6**, 168, <https://doi.org/10.3389/fmars.2019.00168>.
- Dufau, C., M. Orszynowicz, G. Dibarbouré, R. Morrow, and P. Traon, 2016: Mesoscale resolution capability of altimetry: Present and future. *J. Geophys. Res. Oceans*, **121**, 4910–4927, <https://doi.org/10.1002/2015JC010904>.
- Durand, M., L.-L. Fu, D. P. Lettenmaier, D. E. Alsdorf, E. Rodríguez, and D. Esteban-Fernandez, 2010: The Surface Water and Ocean Topography mission: Observing terrestrial surface water and oceanic submesoscale eddies. *Proc. IEEE*, **98**, 766–779, <https://doi.org/10.1109/JPROC.2010.2043031>.
- Eble, M. C., and F. I. Gonzalez, 1991: Deep-ocean bottom pressure measurements in the northeast Pacific. *J. Atmos. Oceanic Technol.*, **8**, 221–233, [https://doi.org/10.1175/1520-0426\(1991\)008<0221:DOBPMI>2.0.CO;2](https://doi.org/10.1175/1520-0426(1991)008<0221:DOBPMI>2.0.CO;2).
- Flament, P., L. Armi, and L. Washburn, 1985: The evolving structure of an upwelling filament. *J. Geophys. Res.*, **90**, 11 765–11 778, <https://doi.org/10.1029/JC090iC06p11765>.
- Fu, L.-L., and A. Cazenave, 2001: *Satellite Altimetry and Earth Sciences*. Academic Press, 509 pp.
- , and C. Uebelmann, 2014: On the transition from profile altimeter to swath altimeter for observing global ocean surface topography. *J. Atmos. Oceanic Technol.*, **31**, 560–568, <https://doi.org/10.1175/JTECH-D-13-00109.1>.
- Gula, J., T. M. Blacic, and R. E. Todd, 2019: Submesoscale coherent vortices in the Gulf Stream. *Geophys. Res. Lett.*, **46**, 2704–2714, <https://doi.org/10.1029/2019GL081919>.
- Guthrie, J., and Coauthors, 2020: Preliminary results from the first deployments of the dynamic ocean topography buoy: In-situ observations of sea surface height in ice-covered seas. *AGU Ocean Sciences Meeting*, San Francisco, CA, Amer. Geophys. Union, Abstract HE14B-1930, <https://agu.confex.com/agu/osm20/meetingapp.cgi/Paper/648899>.
- Haines, B., S. Desai, C. Meinig, and S. Stalin, 2017: CAL/VAL of the SWOT SSH spectrum: Moored GPS approach. *SWOT Science Team Meeting*, Toulouse, France, NASA, <https://trs.jpl.nasa.gov/handle/2014/48164>.
- , —, A. Dodge, R. Leben, M. Shannon, C. Meinig, and S. Stalin, 2019: The Harvest experiment: New results from the platform and moored GPS buoys. *Ocean Surface Topography Science Team Meeting*, Chicago, IL, NASA.
- , —, D. Kubitschek, and R. Leben, 2021: A brief history of the Harvest experiment: 1989–2019. *Adv. Space Res.*, **68**, 1161–1170, <https://doi.org/10.1016/j.asr.2020.08.013>.
- Hersbach, H., and Coauthors, 2020: The ERA5 global reanalysis. *Quart. J. Roy. Meteor. Soc.*, **146**, 1999–2049, <https://doi.org/10.1002/qj.3803>.
- Hickey, B. M., 1979: The California Current system—Hypotheses and facts. *Prog. Oceanogr.*, **8**, 191–279, [https://doi.org/10.1016/0079-6611\(79\)90002-8](https://doi.org/10.1016/0079-6611(79)90002-8).

- Ikedo, M., and W. J. Emery, 1984: Satellite observations and modeling of meanders in the California Current system off Oregon and Northern California. *J. Phys. Oceanogr.*, **14**, 1434–1450, [https://doi.org/10.1175/1520-0485\(1984\)014<1434:SOAMOM>2.0.CO;2](https://doi.org/10.1175/1520-0485(1984)014<1434:SOAMOM>2.0.CO;2).
- Kanzow, T., U. Send, W. Zenk, A. D. Chave, and M. Rhein, 2006: Monitoring the integrated deep meridional flow in the tropical North Atlantic: Long-term performance of a geostrophic array. *Deep-Sea Res. I*, **53**, 528–546, <https://doi.org/10.1016/j.dsr.2005.12.007>.
- LaCasce, J. H., and A. Mahadevan, 2006: Estimating subsurface horizontal and vertical velocities from sea surface temperature. *J. Mar. Res.*, **64**, 695–721, <https://doi.org/10.1357/002224006779367267>.
- Lapeyre, G., and P. Klein, 2006: Dynamics of the upper oceanic layers in terms of surface quasigeostrophy theory. *J. Phys. Oceanogr.*, **36**, 165–176, <https://doi.org/10.1175/JPO2840.1>.
- Li, Z., J. Wang, and L.-L. Fu, 2019: An observing system simulation experiment for ocean state estimation to assess the performance of the SWOT mission: Part 1—A twin experiment. *J. Geophys. Res. Oceans*, **124**, 4838–4855, <https://doi.org/10.1029/2018JC014869>.
- Meinig, C., S. E. Stalin, A. I. Nakamura, and H. B. Milburn, 2005: Real-time deep-ocean tsunami measuring, monitoring, and reporting system: The NOAA DART II description and disclosure. NOAA NDBC Rep., 15 pp.
- Melville, W. K., L. Lenain, D. R. Cayan, M. Kahru, J. P. Kleissl, P. Linden, and N. M. Statom, 2016: The Modular Aerial Sensing System. *J. Atmos. Oceanic Technol.*, **33**, 1169–1184, <https://doi.org/10.1175/JTECH-D-15-0067.1>.
- Mihaly, S. F., R. E. Thomson, and A. B. Rabinovich, 1998: Evidence for nonlinear interaction between internal waves of inertial and semidiurnal frequency. *Geophys. Res. Lett.*, **25**, 1205–1208, <https://doi.org/10.1029/98GL00722>.
- Morrow, R., and Coauthors, 2019: Global observations of fine-scale ocean surface topography with the Surface Water and Ocean Topography (SWOT) mission. *Front. Mar. Sci.*, **6**, 232, <https://doi.org/10.3389/fmars.2019.00232>.
- Osse, T. J., C. Meinig, S. Stalin, and H. Milburn, 2015: The Prowler, a vertical profiler powered by wave energy. *OCEANS 2015*, Washington, DC, IEEE, <https://doi.org/10.23919/OCEANS.2015.7404354>.
- Pinkel, R., M. A. Goldin, J. A. Smith, O. M. Sun, A. A. Aja, M. N. Bui, and T. Huguen, 2011: The Wirewalker: A vertically profiling instrument carrier powered by ocean waves. *J. Atmos. Oceanic Technol.*, **28**, 426–435, <https://doi.org/10.1175/2010JTECHO805.1>.
- Ponte, A. L., and P. Klein, 2015: Incoherent signature of internal tides on sea level in idealized numerical simulations. *Geophys. Res. Lett.*, **42**, 1520–1526, <https://doi.org/10.1002/2014GL062583>.
- Pujol, M. I., Y. Faugère, G. Taburet, S. Dupuy, C. Pelloquin, M. Ablain, and N. Picot, 2016: DUACS DT2014: The new multi-mission altimeter data set reprocessed over 20 years. *Ocean Sci.*, **12**, 1067–1090, <https://doi.org/10.5194/os-12-1067-2016>.
- Qiu, B., S. Chen, P. Klein, J. Wang, H. Torres, L. Fu, and D. Menemenlis, 2018: Seasonality in transition scale from balanced to unbalanced motions in the World Ocean. *J. Phys. Oceanogr.*, **48**, 591–605, <https://doi.org/10.1175/JPO-D-17-0169.1>.
- Quarty, G. D., G. Chen, F. Nencioli, R. Morrow, and N. Picot, 2021: An overview of requirements, procedures and current advances in the calibration/validation of radar altimeters. *Remote Sens.*, **13**, 125, <https://doi.org/10.3390/rs13010125>.
- Ray, R. D., 2013: Precise comparisons of bottom-pressure and altimetric ocean tides. *J. Geophys. Res. Oceans*, **118**, 4570–4584, <https://doi.org/10.1002/jgrc.20336>.
- Rocha, C., T. Chereskin, G. Gille, and D. Menemenlis, 2016: Mesoscale to submesoscale wavenumber spectra in Drake Passage. *J. Phys. Oceanogr.*, **46**, 601–620, <https://doi.org/10.1175/JPO-D-15-0087.1>.
- Rudnick, D. L., K. D. Zaba, R. E. Todd, and R. E. Davis, 2017: A climatology of the California Current system from a network of underwater gliders. *Prog. Oceanogr.*, **154**, 64–106, <https://doi.org/10.1016/j.pocean.2017.03.002>.
- Savage, A. C., and Coauthors, 2017: Spectral decomposition of internal gravity wave sea surface height in global models. *J. Geophys. Res. Oceans*, **122**, 7803–7821, <https://doi.org/10.1002/2017JC013009>.
- Schaeffer, P., and Coauthors, 2018: What do we need to improve the next mean sea surface? *Ocean Surface Topography Science Team Meeting*, Ponta Delgado, Portugal, NASA.
- Strub, P. T., and C. James, 2000: Altimeter-derived variability of surface velocities in the California Current system: 2. Seasonal circulation and eddy statistics. *Deep-Sea Res. II*, **47**, 831–870, [https://doi.org/10.1016/S0967-0645\(99\)00129-0](https://doi.org/10.1016/S0967-0645(99)00129-0).
- Su, Z., and Coauthors, 2018: Ocean submesoscales as a key component of the global heat budget. *Nat. Commun.*, **9**, 775, <https://doi.org/10.1038/s41467-018-02983-w>.
- Taburet, G., A. Sanchez-Roman, M. Ballarotta, M. I. Pujol, J. F. Legeais, F. Fournier, Y. Faugère, and G. Dibarboure, 2019: DUACS DT-2018: 25 years of reprocessed sea level altimeter products. *Ocean Sci.*, **15**, 1207–1224, <https://doi.org/10.5194/os-15-1207-2019>.
- Torres, H. S., P. Klein, D. Menemenlis, B. Qiu, Z. Su, J. Wang, S. Chen, and L. Fu, 2018: Partitioning ocean motions into balanced motions and internal gravity waves: A modeling study in anticipation of future space missions. *J. Geophys. Res. Oceans*, **123**, 8084–8105, <https://doi.org/10.1029/2018JC014438>.
- Wang, J., and L.-L. Fu, 2019: On the long-wavelength validation of the SWOT KaRIn measurement. *J. Atmos. Oceanic Technol.*, **36**, 843–848, <https://doi.org/10.1175/JTECH-D-18-0148.1>.
- , —, B. Qiu, D. Menemenlis, J. T. Farrar, Y. Chao, A. F. Thompson, and M. M. Flexas, 2018: An observing system simulation experiment for the calibration and validation of the Surface Water Ocean Topography sea surface height measurement using in situ platforms. *J. Atmos. Oceanic Technol.*, **35**, 281–297, <https://doi.org/10.1175/JTECH-D-17-0076.1>.
- , —, H. S. Torres, S. Chen, B. Qiu, and D. Menemenlis, 2019: On the spatial scales to be resolved by the Surface Water and Ocean Topography Ka-band radar interferometer. *J. Atmos. Oceanic Technol.*, **36**, 87–99, <https://doi.org/10.1175/JTECH-D-18-0119.1>.
- Watts, D., and H. T. Rossby, 1977: Measuring dynamic heights with inverted echo sounders: Results from MODE. *J. Phys. Oceanogr.*, **7**, 345–358, [https://doi.org/10.1175/1520-0485\(1977\)007<0345:MDHWIE>2.0.CO;2](https://doi.org/10.1175/1520-0485(1977)007<0345:MDHWIE>2.0.CO;2).
- Wunsch, C., and D. Stammer, 1997: Atmospheric loading and the oceanic inverted barometer effect. *Rev. Geophys.*, **35**, 79–107, <https://doi.org/10.1029/96RG03037>.
- Yu, X., A. L. Ponte, S. Elipot, D. Menemenlis, E. D. Zaron, and R. Abernathy, 2019: Surface kinetic energy distributions in the global oceans from a high-resolution numerical model

- and surface drifter observations. *Geophys. Res. Lett.*, **46**, 9757–9766, <https://doi.org/10.1029/2019GL083074>.
- Zaron, E. D., 2019: Baroclinic tidal sea level from exact-repeat mission altimetry. *J. Phys. Oceanogr.*, **49**, 193–210, <https://doi.org/10.1175/JPO-D-18-0127.1>.
- Zhao, Z., and Coauthors, 2019: Decomposition of the multimodal multidirectional  $M_2$  internal tide field. *J. Atmos. Oceanic Technol.*, **36**, 1157–1173, <https://doi.org/10.1175/JTECH-D-19-0022.1>.
- Zhou, B., C. Watson, B. Legresy, M. King, J. Beardsley, and A. Deane, 2020: GNSS/INS-equipped buoys for altimetry validation: Lessons learnt and new directions from the Bass Strait validation facility. *Remote Sens.*, **12**, 3001, <https://doi.org/10.3390/rs12183001>.